

DRAFT VERSION MAY 21, 2021

Typeset using L^AT_EX twocolumn style in AASTeX62Evolution of cold gas at $2 < z < 5$: a blind search for H I and OH absorption lines towards mid-infrared color selected radio-loud AGNsN. GUPTA,¹ R. SRINANAND,¹ G. SHUKLA,¹ J.-K. KROGAGER,^{2,3} P. NOTERDAEME,² F. COMBES,⁴ R. DUTTA,⁵
J. P. U. FYNBO,^{6,7} M. HILTON,⁸ E. MOMJIAN,⁹ K. MOODLEY,⁸ AND P. PETITJEAN²¹*Inter-University Centre for Astronomy and Astrophysics, Post Bag 4, Ganeshkhind, Pune 411 007, India*²*Institut d'astrophysique de Paris, UMR 7095, CNRS-SU, 98bis bd Arago, 75014 Paris, France*³*Department of Astronomy, University of Geneva, Chemin Pegasi 51, 1290 Versoix, Switzerland*⁴*Observatoire de Paris, Collège de France, PSL University, Sorbonne University, CNRS, LERMA, Paris, France*⁵*Dipartimento di Fisica G. Occhialini, Università degli Studi di Milano-Bicocca, Piazza della Scienza 3, 20126 Milano, Italy*⁶*Cosmic Dawn Center (DAWN), University of Copenhagen, Jagtvej 128, DK-2200, Copenhagen N, Denmark*⁷*Niels Bohr Institute, University of Copenhagen, Jagtvej 128, DK-2200, Copenhagen N, Denmark*⁸*Astrophysics Research Centre and School of Mathematics, Statistics and Computer Science, UKZN, Durban 4041, South Africa*⁹*National Radio Astronomy Observatory, Socorro, NM 87801, USA*

Submitted to ApJ

ABSTRACT

We present results from a spectroscopically blind search for associated and intervening H I 21-cm and OH 18-cm absorption lines towards 88 AGNs at $2 \leq z \leq 5$ using the upgraded Giant Metrewave Radio Telescope (uGMRT). The sample of AGNs with 1.4 GHz spectral luminosity in the range, $10^{27-29.3} \text{ W Hz}^{-1}$, is selected using mid-infrared colors and closely resembles the distribution of the underlying quasar population. The search for associated or proximate absorption, defined to be within 3000 km s^{-1} of the AGN redshift, led to one H I 21-cm absorption detection (M1540–1453; $z_{\text{abs}} = 2.1139$). This is only the fourth known absorption at $z > 2$. The detection rate ($1.6_{-1.4}^{+3.8}\%$) suggests low covering factor of cold neutral medium (CNM; $T \sim 100 \text{ K}$) associated with these powerful AGNs. The intervening absorption line search, with a sensitivity to detect CNM in damped Ly α systems (DLAs), has comoving absorption path lengths of $\Delta X = 130.1$ and 167.7 for H I and OH, respectively. The corresponding number of absorber per unit comoving path lengths are ≤ 0.014 and ≤ 0.011 , respectively. The former is at least 4.5 times lower than that of DLAs and consistent with the CNM cross-section estimated using H₂ and C I absorbers at $z > 2$. Our AGN sample is optically fainter compared to the quasars used to search for DLAs in the past. In our optical spectra obtained using the Southern African Large Telescope (SALT) and the Nordic Optical Telescope (NOT), we detect 5 intervening (redshift path ~ 9.3) and 2 proximate DLAs. This is slightly excessive compared to the statistics based on optically selected quasars. The non-detection of H I 21-cm absorption from these DLAs suggests small CNM covering fraction around galaxies at $z > 2$.

Keywords: quasars: absorption lines — interstellar medium

1. INTRODUCTION

H I 21-cm absorption lines in the spectra of radio sources can provide valuable insights into the cold atomic gas ($T \sim 100 \text{ K}$) associated with active galactic nuclei (AGNs) and intervening galaxies along the line of sight. In the former, generally detected within a few 1000 km s^{-1} of the AGN redshift, the matter may

be *associated* with the AGN, its host galaxy, a nearby companion galaxy, outflows driven by its feedback or infalling material. In the latter, the absorbing gas corresponds to the interstellar or circumgalactic medium of an *intervening* galaxy or intragroup medium. The strength of absorption signal does not depend on the distance to the observer. The H I 21-cm absorption line's strength depends both on the H I column density and the spin temperature of the gas. It could thus be an important probe of the properties of cold gas in distant galaxies and investigating its role in fueling the cosmic evolution of star formation rate (SFR) density and that of the luminosity density of AGNs, both of which peak at $z \simeq 2$.

For a long time radio telescopes have receivers capable of observing the H I 21-cm line up to arbitrarily high redshifts. Indeed, H I 21-cm absorption has been searched in AGNs as distant as $z \sim 5.2$ (e.g., Brown & Roberts 1973; Carilli et al. 2007, 1998). But technical limitations imposed by narrow bandwidths, hostile radio frequency environment and limited number of known bright radio AGNs at high- z have prevented large unbiased radio absorption line surveys. Consequently, to date, the majority of H I 21-cm absorption line observations and detections have been based on optically selected samples of AGNs.

For *associated* absorption, AGNs with known redshifts and, preferably with compact radio morphology, have been observed to study the circumnuclear gas which may be fueling the radio activity or impacted by the AGN feedback (e.g., Vermeulen et al. 2003; Gupta et al. 2006; Darling et al. 2011; Curran et al. 2013; Allison et al. 2014; Geréb et al. 2015; Aditya et al. 2016; Dutta et al. 2019; Grasha et al. 2019). Although more than 500 AGNs have been searched for H I 21-cm absorption the vast majority of observations are at $z < 2$ and most of the detections at $z < 1$ (see Morganti & Oosterloo 2018, for a review). Only 3 detections at $z > 2$ are known, the highest redshift being 3.53 (Aditya et al. 2021). Overall, the bulk of detections are towards compact radio sources (detection rate $\sim 30\text{--}50\%$) associated with galaxies having mid-infrared (MIR) colors suggesting gas and dust rich environment (Glowacki et al. 2017; Chandola et al. 2020). Among detections associated with more powerful AGNs (radio luminosity, $\log(L_{1.4\text{GHz}}/(\text{WHz}^{-1})) > 24$), the H I absorption profiles often show signatures of radio jet-ISM interaction in the form of blue-shifted components representing outflowing gas (Maccagni et al. 2017).

For *intervening* H I 21-cm absorption line studies the targets have been sight lines towards quasars, the most powerful AGNs, selected from the large optical spectroscopic surveys such as the Sloan Digital Sky Survey

(SDSS; York et al. 2000). Generally, sight lines with indications of large H I column densities ($N(\text{H I})$) along the sight line suggested by the presence of a damped Ly α system (DLAs; $N(\text{H I}) > 2 \times 10^{20} \text{cm}^{-2}$; e.g., Srianand et al. 2012; Kanekar et al. 2014), a strong Mg II absorption (rest equivalent width, $W_r > 1\text{\AA}$; e.g., Gupta et al. 2012; Dutta et al. 2017a), or a galaxy at small impact parameter (typically $< 30 \text{kpc}$; e.g., Carilli & van Gorkom 1992; Gupta et al. 2010; Borthakur et al. 2010; Reeves et al. 2016; Dutta et al. 2017c) are selected. The vast majority of the observations are sensitive to detecting cold neutral medium (CNM; $T \sim 100 \text{K}$) in $N(\text{H I}) > 5 \times 10^{19} \text{cm}^{-2}$. The detection rates are typically 10-50%, depending crucially on the sample selection criteria (see, for example, Dutta et al. 2017b). Although the highest redshift detection is at $z \sim 3.38$ (Kanekar et al. 2007), the bulk of the reported H I 21-cm detections are associated with gas rich galaxies at $z < 2$. These studies also suggest that the gas traced by DLAs at $z > 2$ is predominantly warm ($T > 1000 \text{K}$).

It is reasonable to expect optically selected samples of AGNs to be affected by dust-bias. Since cold gas is accompanied by dust, the bias is particularly relevant for H I 21-cm absorption line searches. In the case of associated absorption, the dust intrinsic to AGN may remove objects with certain orientation (Type II) or going through the very early stages of evolution. In the case of intervening gas, it can substantially affect our ability to use optically selected samples of DLAs to detect translucent and dense phases of the ISM (Krogager et al. 2016; Geier et al. 2019), and influence the measurements of H I and metal mass densities (Krogager et al. 2019).

The limitations due to dust obscuration can be overcome by selecting AGNs without resorting to any optical color selection scheme or carry out blind searches of H I 21-cm absorption. The latter is becoming possible with various precursor and pathfinder telescopes of Square Kilometre Array (SKA) equipped with wideband receivers. Especially, the upcoming large H I 21-cm absorption line surveys such as the MeerKAT Absorption Line Survey (MALS; Gupta et al. 2017) and First Large Absorption Survey in H I (FLASH; Allison et al. 2017) will characterize the evolution of cold gas without possible selection effects due to dust-bias or from the choice of different methods used to select sight lines in different redshift ranges (see also Grasha et al. 2020). These will also simultaneously search OH 18-cm main lines, providing additional constraints on the evolution of diffuse molecular gas in the ISM (Gupta et al. 2018a; Balashev et al. 2020).

In this paper, we present a spectroscopically blind search of HI 21-cm absorption at $z > 2$ based on a sample of AGNs selected using the mid-infrared (MIR) colors from Wide-field Infrared Survey Explorer (WISE; Wright et al. 2010; Cutri & et al. 2014) and having spectroscopically confirmed redshifts using the Southern African Large Telescope (SALT; 180 hrs) and the Nordic Optical Telescope (NOT; 3 nights; Krogager et al. 2018). Note that similar to the radio waveband the infrared wavelengths are also unaffected by dust obscuration. These AGNs are being observed as part of MALS, which is a large project at the MeerKAT array in South Africa, to search HI 21-cm and OH 18-cm lines at $z < 2$. The upgraded Giant Metrewave Radio Telescope (uGMRT) survey presented here covers $2 < z < 5.1$.

The paper is laid out as follows. In Section 2, we present the sample definition and its properties in the context of previous radio-selected samples to search for DLAs. The details of uGMRT observations and data analysis to obtain the radio spectra and spectral line catalog are presented in Section 3. We provide the details of HI 21-cm absorber detected from the survey in Section 4. In sections 5 and 6, we compute the incidences of intervening and associated HI 21-cm absorption lines, respectively. In Section 5, we apply the same formalism to also derive the incidence of intervening OH absorption. The availability of SALT-NOT spectra allows us to examine the properties of gas along the sight line using Ly α and various metal absorption lines. In particular, for a subset of uGMRT targets ($z_e > 2.7$) through deeper SALT observations we have discovered 6 DLAs and 1 candidate proximate DLA (PDLA i.e., DLA within 3000 km s^{-1} of z_q). In Section 5, we also present the properties of these Ly α and metal line absorbers and discuss the nature of multi-phase ISM in the context of uGMRT survey results. The results and future prospects are summarized in Section 7.

Throughout this paper we use the Λ CDM cosmology with $\Omega_m=0.27$, $\Omega_\Lambda=0.73$ and $H_0=71 \text{ km s}^{-1} \text{ Mpc}^{-1}$.

2. SAMPLE

2.1. Definition and properties

The targets for the uGMRT survey are drawn from the SALT-NOT sample of 303 AGNs constructed for MALS. The SALT-NOT sample is selected on the basis of MIR colors from WISE. We defined the following color wedge based on the first three bands of WISE i.e., W_1 ($3.4 \mu\text{m}$), W_2 ($4.6 \mu\text{m}$), W_3 ($12 \mu\text{m}$),

$$W_1 - W_2 < 1.3 \times (W_2 - W_3) - 3.04; \quad (1)$$

$$W_1 - W_2 > 0.6.$$

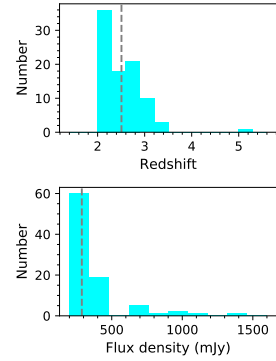


Figure 1. Redshift and flux density (1.4 GHz) distributions for our MIR selected sample. The vertical dashed lines mark the median for each distribution.

As shown in Fig. 1 of Krogager et al. (2018), the MIR-wedge defined above is optimised towards identifying most powerful AGNs (i.e., quasars) at $z > 1.4$.

The details of SALT-NOT target selection process will be presented in a future paper. In short, we cross-correlated AllWISE catalog (Cutri & et al. 2014) and radio sources brighter than 200 mJy in the NRAO VLA Sky Survey (NVSS; Condon et al. 1998), to identify 2011 high-probability quasar candidates satisfying the MIR wedge (Equation 1). We restricted the sample to declination $< +20^\circ$ to ensure reasonable observability with the MeerKAT telescope. A search radius of $10''$ for WISE-NVSS cross-matching was used but all the coincidences were verified using higher spatial resolution quick look radio images at 3 GHz from the Very Large Array Sky Survey (VLASS; Lacy et al. 2020). These quick look images have a spatial resolution of $\sim 2.5''$ and the positional accuracy is limited to $\sim 0.5''$. Consequently, our sample selects preferentially compact core-dominated AGNs. We observed 303 candidates using SALT and NOT to measure redshifts and confirm the AGN nature. This optical spectroscopic campaign has led to a sample of AGNs which can be split into following three categories: (i) with emission lines in the optical spectrum (250 objects with confirmed redshifts at $0.1 < z < 5.1$), (ii) with no emission lines in the optical spectrum (26), and (iii) empty fields i.e., radio continuum peak coincides with the MIR source but neither emission line nor a continuum source are detected in optical spectra and images.

The uGMRT Band-3 covers 250 - 500 MHz which is suitable to search for HI 21-cm absorption over $1.9 < z < 4.7$. It nicely complements the MALS coverage of $z < 1.4$. For the uGMRT survey presented here we selected all the 98 objects at $z > 2$ from the SALT-NOT sample. In the allocated observing time we observed 88 of these which are listed in Table 1.

The redshift (median ~ 2.5) and 1.4 GHz flux density (median ~ 288 mJy) distributions are presented in Fig. 1. The 1.4 GHz spectral luminosities are in the range of $L_{1.4\text{ GHz}} \simeq 10^{27-29.3} \text{ W Hz}^{-1}$. The lower end of luminosity is well above the radio cut-off that separates FRI and FRII radio sources, and the upper end corresponds to the most luminous radio-loud AGN at $z > 5$ discovered from the SALT-NOT survey. All except one are spectroscopically confirmed quasars. The details of radio galaxy M1540-1453 are presented by Shukla et al. (2021).

With the right sample, it is possible to determine the evolution of cold gas in a dust-unbiased way. Therefore, next we examine the efficacy of our sample selection strategy by comparing it with samples of DLAs from radio-selected quasars.

2.2. Comparison with radio-selected DLA samples

The three notable DLA samples based on radio-selected quasars are: (i) the Complete Optical and Radio Absorption Line System (CORALS) survey of 66 QSOs ($z_{em} > 2.2$) by Ellison et al. (2001), (ii) the University of California San Diego (UCSD) survey of 53 QSOs ($z_{em} > 2.0$) for DLAs by Jorgenson et al. (2006), and (iii) the survey of 45 QSOs ($z_{em} > 2.4$) selected from the Texas radio survey (Ellison et al. 2008). These surveys revealed 19, 7 and 9 DLAs over a redshift path, Δz of 57.16, 41.15 and 38.79, respectively. The number of DLAs per unit redshift, n_{DLA} , are estimated to be $0.31^{+0.09}_{-0.08}$, $0.17^{+0.08}_{-0.07}$ and $0.23^{+0.11}_{-0.07}$, respectively. The CORALS survey found a slightly higher incidence of DLAs and suggested that optically-selected DLA samples may be affected by dust-bias. But overall none of the surveys uncovered a population of dusty DLAs.

Targets for these three surveys have been selected at different radio frequencies and to different radio flux limits. While such differences might be subtle, they may still affect the optical properties of the quasars and hence the resulting statistics of DLAs. The CORALS survey has been selected at 2.7 GHz down to a flux density limit of 250 mJy; the UCSD sample has been selected at 4.9 GHz to a flux limit of 350 mJy; and lastly, the survey by Ellison et al. (2008) has been selected at 356 MHz down to a flux density limit of 400 mJy.

In order to compare the effects of the radio-selection, we generate a mock distribution of i -band magnitudes for the three samples as well as for the SALT-NOT sample presented in this work. The intrinsic ultraviolet luminosity function is assumed to be the same in all cases and is taken from the work by Manti et al. (2017). We assume a fixed distribution of the optical-to-radio flux ratio, R_i , following Baloković et al. (2012) as well as

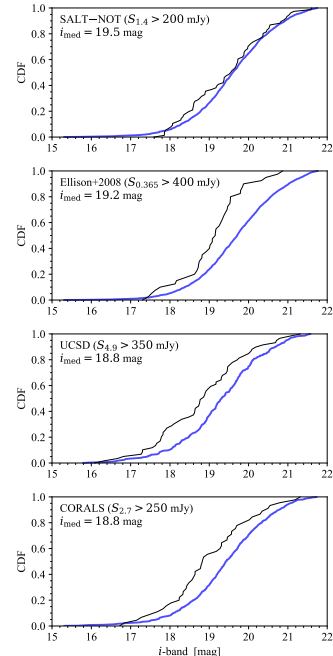


Figure 2. Comparison of optical properties of the high-redshift ($z \gtrsim 2$), radio-selected quasar surveys: SALT-NOT $z > 2$ (this work), Ellison et al. (2008), UCSD (Jorgenson et al. 2006), and CORALS (Ellison et al. 2001). The black line indicates the cumulative distribution of i -band magnitudes in the respective surveys, and the blue line shows the modelled distribution taking into account the survey radio flux limit and spectroscopic follow-up criterion of $B < 22$ mag (see text). The median i -band magnitude of each sample is given in the upper left corner.

a fixed radio slope of $\alpha_\nu = -0.8$, in order to scale the various survey limits to the same frequency (1.4 GHz) as used in our survey and as used by Baloković et al. (2012). Since all the surveys impose roughly the same optical follow-up strategy in order to detect DLAs in low-resolution spectra, we impose a final cut on $B < 22$ mag. For this cut, we use an average color correction for high-redshift QSOs: $B = i + 0.3$ with a scatter of 0.1 mag (see color relations by Krogager et al. 2019). The resulting mock magnitude distribution is shown in Fig. 2 (blue curve) compared to the respective survey data (in black). While all surveys span a wide range of magnitudes, our survey more closely samples the underlying luminosity function and hence introduces a minimal bias in the optical properties of the sample. This is a direct consequence of the fact that SALT-NOT survey has targeted optically fainter quasars (refer to median i -band mags in Fig. 2). An analysis of dust-bias in the sample using optical-infrared colors will be presented in a future paper.

Table 1. Sample of $z > 2$ MIR-selected radio sources (88) observed with uGMRT.

Source name	$F_{1.4\text{ GHz}}$ (mJy)	z_{em}	Obs. run	Beam	$F_{P,420\text{ MHz}}$ (mJy b ⁻¹)	$F_{P,420\text{ MHz}}/F_{420\text{ MHz}}$	$\alpha_{0.4}^{1.4}$	$\alpha_{\nu,band}$	ΔF (mJy b ⁻¹)	N_{cand}	
(1)	(2)	(3)	(4)	(5)	(6)	(7)	(8)	(9)	(10)	(11)	(12)
M004243.06+124657.6	635.0	2.150	16SEP	$7.0'' \times 6.3'', -12.0^\circ$	1628.8	1882.5	0.87	-0.87	-0.86	1.9	-
M005315.65-070233.4	248.2	2.130	16SEP	$7.3'' \times 6.5'', +17.0^\circ$	546.1	536.5	1.02	-0.62	-0.61	2.8	-
M013047.38-172505.6	250.3	2.528	14SEP	$9.9'' \times 6.9'', +40.0^\circ$	532.4	560.2	0.95	-0.64	-0.66	1.5	-
M021231.86-382256.6	244.5	2.260	14SEP	$17.5'' \times 6.8'', +33.0^\circ$	495.7	605.4	0.82	-0.72	-0.71	1.6	1
M022613.72+093726.3	374.6	2.605	14SEP	$8.9'' \times 7.0'', +87.0^\circ$	435.1	436.6	1.0	-0.12	-0.02	2.1	-
M022639.92+194110.1	209.8	2.190	14SEP	$10.4'' \times 6.7'', -83.0^\circ$	390.5	381.7	1.02	-0.48	-0.41	1.9	-
M024939.93+044028.9	420.5	2.008	17SEP	$9.1'' \times 7.6'', +89.0^\circ$	927.7	992.7	0.93	-0.69	-0.67	1.6	-
M025035.54-262743.1	389.2	2.918	17SEP	$11.0'' \times 6.7'', +25.0^\circ$	389.6	419.0	0.93	-0.06	+0.01	1.7	1
M032808.59-015220.2	221.9	2.679	17SEP	$12.0'' \times 8.0'', +72.0^\circ$	370.2	527.3	0.70	-0.69	-0.63	1.3	-
M041620.54-333931.3	264.1	3.045	08SEP	$17.5'' \times 9.0'', -42.0^\circ$	130.0	117.8	1.1	+0.64	+0.51	1.7	-
M042248.53-203456.6	224.3	2.582	08SEP	$11.8'' \times 8.4'', -58.0^\circ$	187.3	192.1	0.98	+0.12	+0.16	1.7	1
M044849.48-093531.3	240.9	2.079	14SEP	$9.3'' \times 7.2'', +46.0^\circ$	152.5	147.3	1.04	+0.39	+0.39	1.6	-
M050725.04-362442.9	212.4	2.930	08SEP	$15.9'' \times 9.6'', -35.0^\circ$	494.5	474.5	1.04	-0.64	-0.51	1.6	-
M051240.99+151723.8	966.5	2.568	07SEP	$6.8'' \times 6.5'', -79.0^\circ$	560.1	595.9	0.94	+0.39	+0.27	1.8	-
M051340.03+010023.6	447.0	2.673	07SEP	$7.7'' \times 6.6'', +64.0^\circ$	342.5	349.7	0.98	+0.20	-0.04	2.1	4
M051511.18-012002.4	288.8	2.287	07SEP	$8.9'' \times 6.4'', +59.0^\circ$	412.5	641.5	0.64	-0.64	-0.68	1.6	1
M051656.35+073252.7	231.7	2.594	07SEP	$10.6'' \times 6.9'', +90.0^\circ$	44.2	44.1	1.0	+1.32	+1.10	1.9	-
M052318.55-261409.6	1354.9	3.110	08SEP	$12.0'' \times 9.1'', -52.0^\circ$	477.7	451.8	1.06	+0.88	+1.08	2.2	-
M061038.80-230145.6	360.2	2.829	14SEP	$11.0'' \times 7.0'', +31.0^\circ$	130.5	129.0	1.01	+0.82	+0.89	1.7	-
M061856.02-315835.2	346.1	2.134	09SEP	$10.8'' \times 6.3'', +0.0^\circ$	877.1	828.6	1.06	-0.70	-0.35	2.0	1
M063602.28-311312.5	262.1	2.654	09SEP	$19.2'' \times 11.1'', +33.0^\circ$	178.7	162.4	1.1	+0.38	+0.42	3.1	-
M063613.53-310646.3	208.0	2.757	09SEP	$11.6'' \times 6.9'', +17.0^\circ$	436.2	474.2	0.92	-0.66	-0.73	2.1	-
M065254.73-323022.6†	322.1	2.239	08SEP	$11.4'' \times 10.1'', +5.0^\circ$	475.9	611.1	0.78	-0.85	-0.95	2.3	-
M070249.30-330205.0	314.6	2.410	08SEP	$12.3'' \times 9.8'', +33.0^\circ$	279.0	328.2	0.85	-	-	2.3	-
M073159.01+143336.3	316.5	2.632	16SEP	$8.8'' \times 8.1'', -49.0^\circ$	574.9	599.8	0.96	-0.52	-0.52	2.8	1
M073714.60-382841.9	219.3	2.107	14SEP	$14.5'' \times 6.6'', +18.0^\circ$	180.0	185.4	0.97	+0.43	+0.40	7.8	-
M080804.34+005708.2	317.0	3.133	08SEP	$14.3'' \times 7.1'', -73.0^\circ$	498.9	515.3	0.97	-0.68	-0.67	2.4	-
M081936.62-063047.9	280.0	2.507	08SEP	$11.9'' \times 6.7'', -73.0^\circ$	434.8	450.7	0.96	-0.28	-0.26	2.1	-
M085826.92-260721.0	404.5	2.036	09SEP	$17.3'' \times 8.5'', -19.0^\circ$	339.0	354.9	0.96	-0.19	-0.08	2.3	-
M090910.66-163753.8	340.1	2.475	09SEP	$9.0'' \times 7.3'', -11.0^\circ$	561.0	523.9	1.07	-0.21	-0.28	2.6	-
M091051.01-052626.8†	337.9	2.395	16SEP	$9.6'' \times 7.2'', -44.0^\circ$	776.2	909.7	0.85	-0.79	-0.94	1.7	-
M095231.66-245349.1	209.5	2.626	14SEP	$10.4'' \times 7.0'', +5.0^\circ$	151.4	166.3	0.91	+0.20	+0.29	1.6	-
M100715.18-124746.7	381.1	2.113	16SEP	$7.7'' \times 6.2'', -24.0^\circ$	80.0	97.3	0.82	-	-	1.6	-
					224.2	210.3	1.07	-0.00	-0.17	1.8	-
					476.6	470.0	1.01	-0.17	-0.21	2.1	-

Table 1 continued

Table 1 (continued)

Source name	$F_{1.4\text{ GHz}}$ (mJy)	z_{em}	Obs. run	Beam	$F_{P,420\text{ MHz}}$ (mJy b $^{-1}$)	$F_{420\text{ MHz}}$ (mJy)	$F_{P,420\text{ MHz}}/F_{420\text{ MHz}}$	$\alpha_{0.4}^{1.4}$	α_{inband}	ΔF (mJy b $^{-1}$)	$N_{Ca\text{ nd}}$
(1)	(2)	(3)	(4)	(5)	(6)	(7)	(8)	(9)	(10)	(11)	(12)
M101313.10-254654.7	248.8	2.965	14SEP	$10.6'' \times 6.9'', +10.0^\circ$	216.7	218.6	0.99	+0.10	-0.0	2.1	-
M102548.76-042933.0	363.5	2.292	16SEP	$6.9'' \times 6.7'', +89.0^\circ$	356.3	391.6	0.91	-0.06	-0.03	2.5	-
M104314.53-232317.5	212.1	2.881	07SEP	$8.9'' \times 6.5'', -10.0^\circ$	460.6	505.8	0.91	-0.69	-0.79	2.2	-
M111820.61-305459.0	233.2	2.352	08SEP	$18.5'' \times 8.4'', -51.0^\circ$	64.8	70.0	0.93	+0.96	+0.10	3.0	-
M111917.36-052707.9	1174.4	2.651	07SEP	$7.1'' \times 6.3'', -48.0^\circ$	1696.6	1793.2	0.95	-0.34	-0.47	3.6	-
M112402.56-150159.1	261.9	2.551	07SEP	$9.0'' \times 6.9'', -23.0^\circ$	194.7	196.0	0.99	+0.23	+0.01	2.6	-
M114226.58-263313.7	294.7	3.237	08SEP	$15.5'' \times 8.3'', -56.0^\circ$	293.6	340.7	0.86	-0.35	-0.31	4.0	-
M115222.04-270126.3	238.2	2.703	08SEP	$13.3'' \times 8.6'', -60.0^\circ$	410.4	441.4	0.93	-0.49	-0.64	2.5	-
M115306.72-044254.5 \dagger	684.8	2.591	16SEP	$7.0'' \times 6.5'', +86.0^\circ$	929.3	899.1	1.03	-0.78	-0.89	2.7	-
M120632.23-071452.6	698.8	2.263	16SEP	$8.0'' \times 6.2'', -9.0^\circ$	980.1	912.2	1.07	-	-	2.7	-
M121514.42-062803.5	360.4	3.218	16SEP	$9.2'' \times 6.6'', -8.0^\circ$	1402.8	1267.9	1.10	-0.48	-0.60	2.7	-
M123150.30-123637.5	276.0	2.106	07SEP	$7.2'' \times 6.5'', -17.0^\circ$	511.1	461.5	1.11	-0.20	-0.31	2.8	-
M123410.08-332638.5	297.9	2.820	08SEP	$15.8'' \times 9.7'', -57.0^\circ$	159.7	205.1	0.78	+0.24	+0.36	1.8	-
M124448.99-044610.2	384.9	3.104	16SEP	$9.1'' \times 7.7'', +28.0^\circ$	665.4	710.4	0.94	-0.69	-0.72	3.4	-
M125442.98-383356.4	219.2	2.776	17SEP	$14.7'' \times 7.0'', +7.0^\circ$	677.2	616.1	1.1	-0.38	-0.40	2.3	1
M125611.49-214411.7	260.7	2.178	16SEP	$10.3'' \times 6.5'', +13.0^\circ$	297.4	300.9	0.99	-0.25	-0.25	2.3	-
M131207.86-202652.4	778.1	5.064	16SEP	$10.5'' \times 6.7'', +21.0^\circ$	446.8	455.4	0.98	-0.45	-0.15	1.7	-
M132657.20-280831.4	404.5	2.238	16SEP	$15.8'' \times 13.8'', -38.0^\circ$	1727.9	1721.9	1.0	-0.63	-0.62	2.0	1
M135131.98-101932.9	726.1	2.999	16SEP	$15.0'' \times 7.0'', +20.0^\circ$	-	2577.0 \dagger	-	-	-	-	-
M141327.20-342235.1	274.7	2.812	09SEP	$9.2'' \times 7.0'', +47.0^\circ$	671.3	874.8	0.77	-0.62	-0.83	2.7	-
M143709.04-294718.5	273.8	2.331	09SEP	$20.9'' \times 6.7'', -42.0^\circ$	1338.3	1886.5	0.71	-0.76	-0.79	2.0	-
M144851.10-112215.6	455.5	2.630	07SEP	$14.6'' \times 7.0'', -44.0^\circ$	78.2	76.4	1.02	+1.02	+0.81	3.9	-
M145342.95-132735.2	254.5	2.370	07SEP	$7.3'' \times 6.0'', -48.0^\circ$	333.0	456.1	0.73	-0.41	-0.49	2.5	-
M145502.84-170014.2	294.7	2.291	07SEP	$7.6'' \times 6.2'', -33.0^\circ$	967.0	896.8	1.08	-0.54	-0.71	3.1	1
M145625.83+045645.2	287.9	2.134	09SEP	$7.6'' \times 6.2'', -33.0^\circ$	477.3	634.7	0.75	-0.73	-0.83	2.2	-
M145908.92-164542.3	378.9	2.006	07SEP	$8.3'' \times 6.4'', -13.0^\circ$	345.8	352.2	0.98	-0.14	-0.23	2.3	-
M150425.30+081858.6	210.8	2.035	09SEP	$7.1'' \times 6.8'', +87.0^\circ$	800.8	813.2	0.98	-0.83	-0.82	2.6	-
M151129.01-072255.3	326.3	2.582	17SEP	$8.5'' \times 6.6'', -9.0^\circ$	853.1	909.6	0.94	-0.70	-0.85	2.1	-
M151304.72-252439.7 \dagger	217.6	3.132	09SEP	$8.4'' \times 7.6'', -32.0^\circ$	122.1	138.5	0.88	+0.34	+0.27	4.8	-
M151944.77-115144.6	441.0	2.014	17SEP	$7.8'' \times 6.8'', -85.0^\circ$	672.7	624.9	1.08	-0.52	-0.71	2.7	-
M154015.23-145341.5	203.3	2.098	17SEP	$9.1'' \times 6.8'', +1.0^\circ$	855.7	819.4	1.04	-1.26	-1.26	3.6	-
M155825.35-215511.1	206.9	2.760	09SEP	$9.2'' \times 7.6'', +84.0^\circ$	268.5	242.1	1.11	-	-	3.6	-
M161907.44-093952.5	340.3	2.891	17SEP	$9.2'' \times 7.6'', +84.0^\circ$	425.0	561.5	0.76	-0.19	-0.01	3.7	-
M162047.94+003653.2	317.8	2.438	17SEP	$9.8'' \times 7.5'', +61.0^\circ$	642.4	595.0	1.08	-0.86	-0.98	2.6	1
M164950.51+062653.3	389.2	2.144	17SEP	$13.7'' \times 6.7'', -42.0^\circ$	209.5	235.8	0.89	-0.10	+0.09	3.0	-
				$8.9'' \times 6.8'', +66.0^\circ$	757.0	695.5	1.09	-0.57	-0.43	2.2	-
				$10.7'' \times 7.6'', +2.0^\circ$	226.9	234.3	0.97	+0.24	+0.16	3.3	-
				$13.6'' \times 9.3'', -11.0^\circ$	154.3	204.3	0.76	+0.51	+0.36	2.6	-

Table 1 continued

Table 1 (continued)

Source name	$F_{1.4\text{ GHz}}$ (mJy)	z_{em}	Obs. run	Beam	$F_{P,420\text{ MHz}}$ (mJy b $^{-1}$)	$F_{420\text{ MHz}}$ (mJy)	$F_{P,420\text{ MHz}}/F_{420\text{ MHz}}$	$\alpha_{0.4}^{1.4}$	α_{inband}	ΔF (mJy b $^{-1}$)	N_{cand}
(1)	(2)	(3)	(4)	(5)	(6)	(7)	(8)	(9)	(10)	(11)	(12)
M165038.03-124854.5	275.5	2.527	09SEP	$7.3'' \times 6.2'', -20.0^\circ$	729.6	675.1	1.08	-0.72	-0.52	5.0	-
M165435.38+001719.2	255.3	2.363	07SEP	$9.2'' \times 7.3'', -14.0^\circ$	405.7	381.5	1.06	-0.32	-0.44	4.2	-
M194110.28-300720.9	315.0	2.059	17SEP	$23.6'' \times 8.3'', +51.0^\circ$	164.0	227.2	0.72	+0.26	+0.40	3.6	-
M200209.37-145531.8	620.3	2.192	17SEP	$8.6'' \times 7.1'', -17.0^\circ$	942.0	896.1	1.05	-0.29	-0.31	2.9	-
M201708.96-293354.7	327.2	2.617	17SEP	$20.5'' \times 7.3'', +50.0^\circ$	1044.7	1201.1	0.87	-1.04	-1.02	2.7	1
M203425.65-052332.2	419.7	2.070	17SEP	$8.0'' \times 7.3'', +85.0^\circ$	366.2	407.2	0.9	+0.02	+0.10	4.0	-
M204737.67-184141.2	241.7	2.994	16SEP	$13.8'' \times 6.7'', -49.0^\circ$	273.0	284.3	0.96	-0.13	-0.17	2.2	-
M205245.03-223410.6	330.9	2.072	16SEP	$12.3'' \times 6.0'', -41.0^\circ$	631.8	608.3	1.04	-0.49	-0.60	3.5	-
M210143.29-174759.2	959.5	2.803	16SEP	$9.5'' \times 5.8'', -39.0^\circ$	2554.1	2477.5	1.03	-0.76	-0.91	3.6	-
M212821.83-150453.2	245.5	2.547	17SEP	$9.2'' \times 6.9'', +6.0^\circ$	443.4	460.8	0.96	-0.50	-0.49	2.0	-
M220127.50+031215.6	300.5	2.181	17SEP	$18.3'' \times 8.6'', +77.0^\circ$	180.5	191.6	0.94	+0.36	+0.33	1.7	-
M222332.81-310117.3	231.7	3.206	17SEP	$25.0'' \times 9.2'', +40.0^\circ$	230.6	330.2	0.7	-0.28	-0.40	2.6	-
M223816.27-124036.4	213.6	2.623	16SEP	$12.3'' \times 8.3'', -50.0^\circ$	464.3	435.5	1.07	-0.57	-0.65	3.7	-
M224111.48-244239.0	211.4	2.242	16SEP	$10.9'' \times 6.1'', -31.0^\circ$	255.0	254.8	0.99	-0.15	-0.17	2.2	-
M224705.52+121151.4	223.7	2.185	14SEP	$12.1'' \times 7.5'', +83.0^\circ$	474.3	489.1	0.97	-0.62	-0.60	1.9	-
M224950.57-263459.6	228.8	2.174	16SEP	$9.8'' \times 5.7'', -23.0^\circ$	568.3	542.1	1.05	-0.69	-0.59	2.4	-
M230036.41+194002.9	210.4	2.160	17SEP	$27.7'' \times 8.2'', +79.0^\circ$	475.8	556.0	0.86	-0.78	-0.65	11.2	-
M231634.61+042940.2	214.0	2.180	16SEP	$6.9'' \times 6.6'', +47.0^\circ$	103.3	97.9	1.06	+0.70	+0.50	3.0	-
M234910.12-043803.2	206.1	2.240	16SEP	$7.7'' \times 6.8'', -62.0^\circ$	168.3	185.6	0.91	+0.08	-0.04	5.1	-
M235722.47-073134.3	235.5	2.764	16SEP	$7.0'' \times 6.0'', -19.0^\circ$	372.4	398.2	0.94	-0.42	-0.40	2.4	-

NOTE— Column 1: source name based on right ascension and declination (J2000) from NVSS. Column 2: 20 cm flux density from NVSS. Column 3: emission line redshift measured from SALT-NOT survey. Column 4: observing run (see Table 2). Note that only M1312-2026 was also observed at Band-2. Columns 5 – 7: synthesised beam, peak of the prominent Gaussian component and total flux densities, respectively, from the continuum image based on 390–450 MHz range (average 420 MHz). Column 8: ratio of columns 6 and 7. Column 9: spectral index derived using NVSS and 420 MHz flux densities. In a few cases, which are all sources with a single component fit, this ratio marginally ($\sim 5\%$) exceeds 1, suggesting that the radio emission may be partially resolved. Column 10: in-band spectral index. Column 11: observed spectral rms at 420 MHz. Column 12: number of absorption candidates.

‡: The radio source is double lobed in 420 MHz image (see Section 3.1 for details). †: Corresponds to Band-2.

3. OBSERVATIONS AND DATA ANALYSIS

3.1. Observations

We used the recently commissioned **Band-2** (120-240 MHz) and **Band-3** (250-500 MHz) of uGMRT to observe redshifted associated and intervening H I 21-cm absorption lines from the sample. The total allocated time including all overheads for the survey observations was 90 hrs.

The **Band-3** observations were split into 6 observing runs in September, 2018 (see Table 2). For these, we used GMRT Wideband Backend (GWB) with a baseband bandwidth of 200 MHz covering 300-500 MHz and split into 8192 frequency channels. This corresponds to a redshift coverage of 1.84 - 3.73 for H I 21-cm line. The channel resolution is 24.414 kHz, which at 400 MHz provides a velocity resolution of 18.3 km s^{-1} . Each target was observed for typically 30-45 mins. The details of which target sources were visited in which observing run are summarized in column 4 of Table 1.

For **Band-2** observations which targeted only M1312-2026, the highest redshift quasar in the sample, the GMRT Software Backend (GSB) was used to configure a baseband bandwidth of 4.17 MHz split into 512 spectral channels. The observing band was centered at 234.1 MHz (resolution $\sim 10 \text{ km s}^{-1}$), the redshifted H I 21-cm line frequency of the source. The total on-source time was 4.2 hrs.

Additionally, five absorption candidates identified from the **Band-3** survey observations were reobserved on December 10, 2019 and February 20, 2020. We used GWB with a bandwidth of 6.25 MHz centered at line frequency (details in Section 3.3) and split into 4096 channels (resolution $\sim 1 \text{ km s}^{-1}$). Each candidate was observed for 3 hrs (on-source time ~ 2.2 hrs).

For all the observations, only parallel hand correlations RR and LL were obtained. During each observing run 3C48, 3C147 and/or 3C286 were observed for flux density and bandpass calibrations. A complex gain calibrator was also observed for each target source.

3.2. Data analysis

All the data were edited, calibrated and imaged using the Automated Radio Telescope Imaging Pipeline (ARTIP) following the steps described in Gupta et al. (2021). After flagging and calibration, the spectral line processing of wideband **Band-3** data was sped up by partitioning the 200 MHz bandwidth into four 50 or 60 MHz wide spectral windows with an overlap of 10 MHz between the adjacent windows. These spectral windows covered: 300-360 MHz, 350-410 MHz, 400-460 MHz and 450-500 MHz. The calibrated visibilities for each spectral window were processed separately (in-

Table 2. Details of uGMRT observations.

Run ID	Band	Date [†]	Duration [‡]
Survey observations			
21APR	Band-2	2018 April 21	7
07SEP	Band-3	2018 September 07	11
08SEP	"	2018 September 08	10
09SEP	"	2018 September 09	11
14SEP	"	2018 September 14	10
16SEP	"	2018 September 16	21
17SEP	"	2018 September 17	20
Follow-up observations			
10DEC	"	2019 December 10	6
20FEB	"	2020 February 20	9

NOTE— †: Start date as per Indian Standard Time. ‡: In hours.

dependently) for RFI flagging, continuum imaging and self-calibration, and continuum subtraction. The continuum subtracted visibilities were imaged to obtain RR and LL spectral line cubes. For this a ‘common’ synthesized beam corresponding to the lowest frequency spectral window was used.

The narrow band datasets from **Band-2** survey and **Band-3** follow-up observations were processed as a single 4.17 or 6.25 MHz wide spectral window, respectively.

3.2.1. Continuum analysis

For **Band-3**, the spectral window covering 390-450 MHz, hereafter identified through the central reference frequency of 420 MHz, is least affected by RFI resulting in best possible continuum images from the data. We used CASA task IMFIT to model the radio continuum emission in these images as multiple Gaussian components. The 9 cases requiring more than one Gaussian component are shown in Fig. 3. Only in 4 cases i.e., M0652–3230, M0910–0526, M1153–0442 and M1513–2524, does the second component contains more than 20% of the total flux density.

In columns 5 and 6 of Table 1 we list synthesized beams and peak flux densities of the most prominent Gaussian component. For the above-mentioned four sources the second component is also listed. In the remaining cases the additional components are too faint ($< 50 \text{ mJy}$) to be useful for the objectives of this paper, hence we do not list their individual properties. The total flux density as estimated from the single or multiple component fit is provided in column 7.

In Fig. 3, we also show optical images from Pan-STARRS1 (PS1) (Chambers et al. 2016). Note that

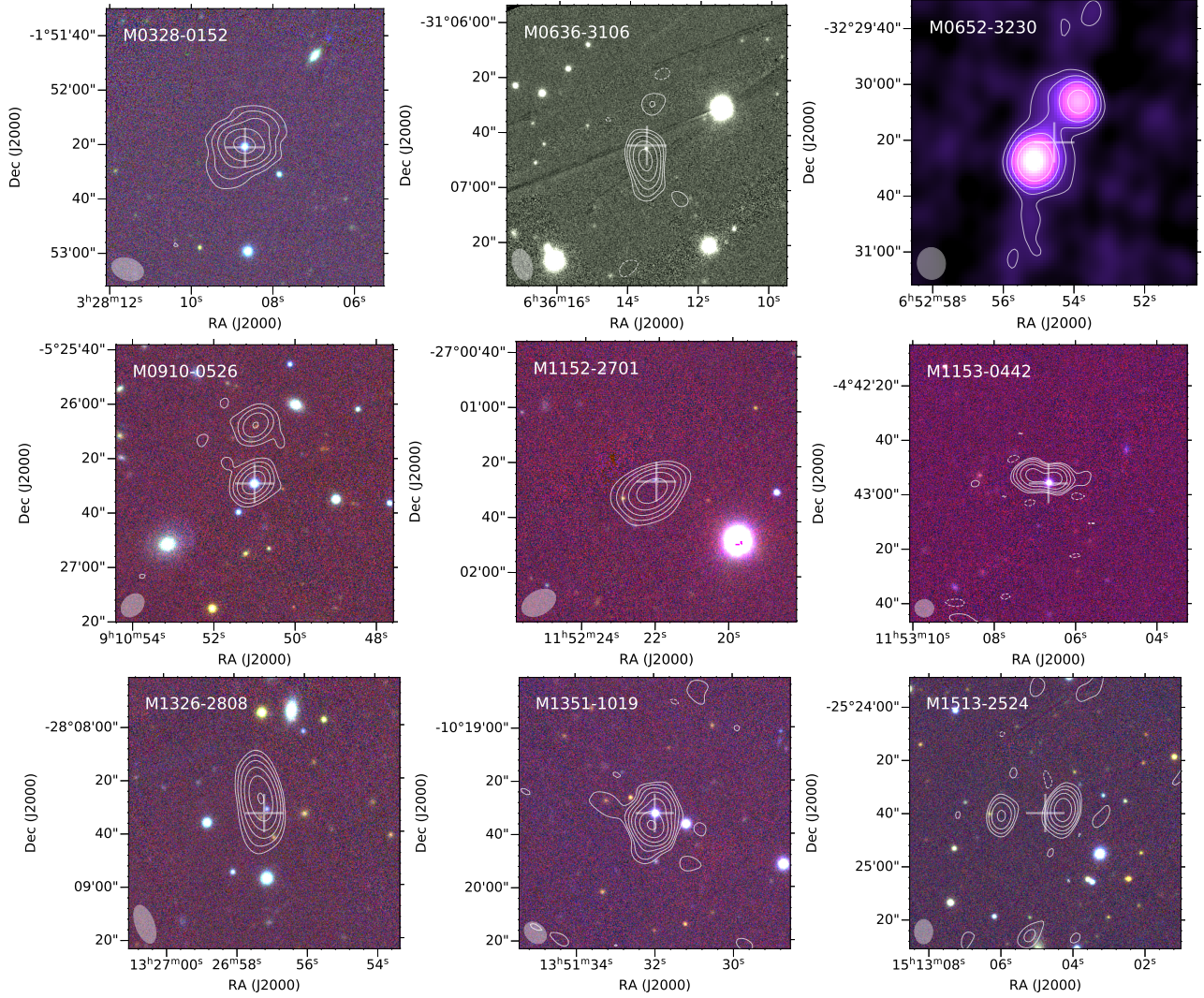


Figure 3. uGMRT radio continuum (420 MHz) contours overlaid on PS1 *yig* color composite images. For M0636-3106 and M0652-3230, the background image is PS1 *i*-band and uGMRT 420 MHz, respectively. The contour levels are shown at $20 \times (-1, 1, 2, 4, 8, \dots)$ mJy beam $^{-1}$. The synthesized beams, shown at the bottom-left corner of images, and the peak and total flux densities are provided in column 5 - 7 of Table 1, respectively. The position of WISE source is marked with a cross.

M0652-3230 is too south to be covered in PS1. The location of MIR sources from WISE are also shown in the images. Owing to the MIR-selection wedge described in Section 2, all but one radio source in our sample are quasars (see Section 2.1 for details). Indeed the median spectral index¹, $\alpha_{0.4}^{1.4}$, derived using the NVSS 1420 MHz and the uGMRT 420 MHz total flux densities is -0.38 (see column 9 of Table 1 and Fig. 4). As expected this is flatter than the overall radio source population which has $\alpha \sim -0.8$. Thus, for our sample, when radio emission is dominated by a single component, we expect AGN to be located close to the peak of the radio emission. In case two prominent radio components are

present i.e., a compact symmetric object (CSO; Conway 2002) morphology, the AGN is expected to be located in between them. In all but 2 cases (M0910-0526 and M1513-2524; details provided below), the optical / MIR counterpart is at the location of the AGN expected from the radio morphology. As previously mentioned we have also verified these coincidences using higher spatial resolution 3 GHz VLASS images.

In the case of M0910-0526, the northern component could be an unrelated radio source (Fig 3). We will exclude this component from the absorption line statistics. M1513-2524, the only radio galaxy in the sample presented here, is among the optically faintest ($r > 23$ mag) in our survey. Among the two radio components, one of them is closer to the MIR source (see Fig 3). We have tentatively detected faint radio emission i.e., radio core

¹ Spectral index α is defined by the power law, $S_\nu \propto \nu^\alpha$

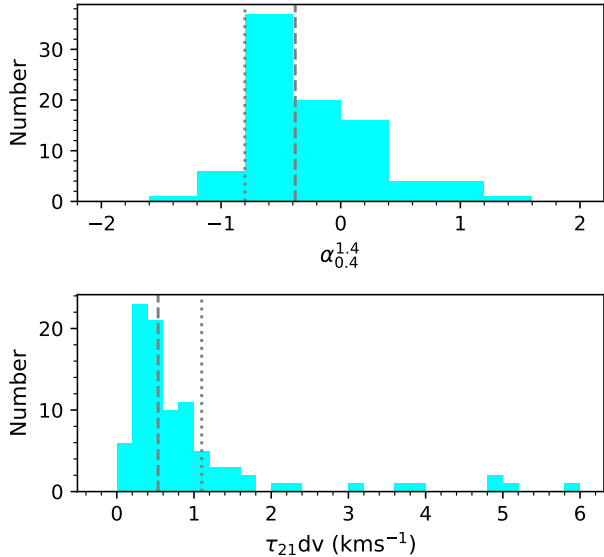


Figure 4. Distributions of radio spectral index between 1400 and 420 MHz ($\alpha_{0.4}^{1.4}$) and 5σ 21-cm optical depth ($\int \tau dv$). The vertical dashed lines mark the median for each distribution. The dotted lines correspond to $\alpha = -0.8$ and $\tau_{21} dv = 1.1 \text{ km s}^{-1}$.

at the location of the MIR source. For details see higher spatial resolution radio images presented in [Shukla et al. \(2021\)](#). We will consider the eastern and western radio components as the two radio lobes of this radio galaxy.

For M1312–2026, the only target also observed in **Band-2**, the properties at 234 MHz are also provided in [Table 1](#). The associated radio emission is compact with a deconvolved size of $15.8'' \times 13.8''$ (position angle = -38.0°). Based on the observed flux densities, M1312-2026, has a spectral luminosity of $L(1.4 \text{ GHz}) = 1.2 \times 10^{29} \text{ W Hz}^{-1}$, which is more than three orders of magnitude higher than the radio power cut-off that separates FRI and FRII radio sources, and greater than the luminosity of any known radio-loud AGN at $z > 5$. The multi-frequency VLA and VLBA observations of this AGN have been obtained to investigate its radio morphology.

3.3. Spectral line analysis

For spectral line analysis, RR and LL spectra in the *heliocentric* frame were extracted at the location of radio continuum peaks from the spectral line cubes. The spectra show systematic oscillations or ripples due to residual bandpass calibration, and numerous positive/negative spikes (for an example see [Fig. 5](#)). The ripple is not identical in the two parallel hands and also varies from one target source to other. We removed its effect by iteratively fitting the underlying structure using Savitsky-Golay filtering with `window length = 24`

and `polynomial order = 3`. In each iteration, the pixels deviating beyond the threshold were flagged and excluded from the subsequent iterations. The continuum was interpolated across the masked pixels and the process was repeated until no deviant pixels were found.

The above determined continuum fit was subtracted from the RR and LL spectra, and an error spectrum was generated by calculating a rolling standard deviation (σ_{rolling} ; window size=48 channels). For **Band-3**, an additional step was to merge the spectra from adjacent spectral windows and unmask the spikes to obtain the final RR and LL spectra covering the entire 300–500 MHz. These were then averaged with appropriate statistical weights to obtain the final Stokes-*I* spectra. The resultant Stokes-*I* spectra have flat baselines but numerous positive and negative spikes (for example see [Fig. 6](#)).

The **Band-2** spectrum of M1312–2026 is presented in [Fig. 7](#). These data were severely affected by the radio frequency interference (RFI). The broad-band RFI mostly affected the shorter baselines ($< 4 \text{ k}\lambda$) which were completely flagged. There was also narrow-band impulse-like bursts of RFI, which affected all the baselines. Overall $\sim 55\%$ of the data was flagged due to antenna/baseline-based problems and RFI. The spectral rms in the Stokes-*I* spectrum presented here is 8.5 mJy/beam , which for the unsmoothed spectrum presented here corresponds to a 1σ optical depth sensitivity of 0.003. There are several statistically significant narrow-band features with widths of 1–2 spectral channels detected in the spectrum. But all of these are coincident with the spikes present in the RFI-spectrum, and are most likely due to the low-level narrow-band RFI which could not be detected in the individual baselines.

In general, no true emission is expected in our spectra and only a tiny fraction of negative spikes are expected to represent true absorption. The majority of these spikes are RFI artefacts. The biggest issue in spectral line search at low frequencies is to distinguish between true absorption and RFI artefacts. The rest of this section is concerned with absorption line search in **Band-3** spectra.

The worst RFI in **Band-3** spectra (e.g., at 360–380 MHz) was flagged by applying an initial mask prior to any calibration (see shaded regions in [Fig. 6](#)). Further, to identify artefacts due to weaker but persistent RFI, we generated median Stokes-*I* spectra for each observing run and the full survey. The median spectrum from the survey and 08SEP run in which M0422-2034 was observed are shown in [Fig. 6](#). The pixels deviating by more than 5σ in the median spectra were taken to represent RFI artefacts. We rejected corresponding

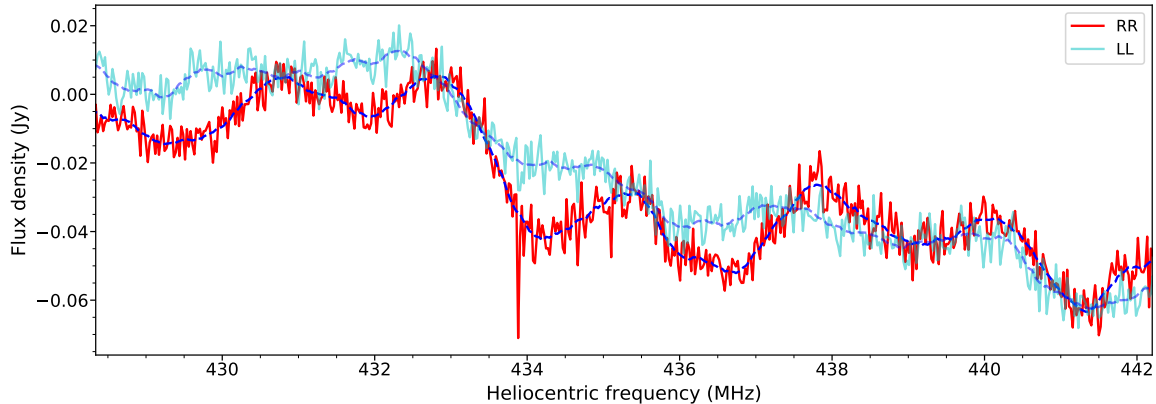


Figure 5. RR and LL spectra of M1206-0714 and continuum fits (dashed line).

pixels in the individual source spectrum. In Fig. 6, such pixels for M0422-2034 are plotted in red.

After this we created a list of 550 absorption line candidates using a detection algorithm which requires: (i) flux density at a pixel j , $F(j) < -5 \times \sigma_{\text{rolling}}(j)$ and (ii) Heliocentric frequency at j , $\nu(j) \geq \nu_{21\text{cm}} / (1 + (z_{em} + 0.01))$, where $\nu_{21\text{cm}}$ is the rest-frame 21-cm line frequency. The factor of 0.01 in the denominator, which approximately corresponds to a outflowing velocity of $\sim 3000 \text{ km s}^{-1}$, allows for the possibility of detecting redshifted absorption associated with AGN (see Fig. 21 of Gupta et al. 2006).

Next, we created a false-detection spectrum by identifying pixels based on following two characteristics. First, we identified all positive spikes with $F(j) > 5 \times \sigma_{\text{rolling}}(j)$. These are unphysical and hence false detections because HI emission lines are too weak to be detectable at $z > 2$ in our spectra. Second, we identified all negative spikes i.e., $F(j) < -5 \times \sigma_{\text{rolling}}$ but only at $\nu(j) < \nu_{21\text{cm}} / (1 + (z_{em} + 0.01))$. These are unphysical because absorbing gas must be in the front of radio source. In Fig. 6, we mark three candidates using \star . Two of these are clearly false detections whereas third one at 395.5 MHz (approximately $+800 \text{ km s}^{-1}$ with respect to z_{em}) could be a true absorption associated with the AGN. The cumulative distributions of all the false absorption (528) and emission (1359) detections from the survey are shown in Fig. 8. These represent frequency ranges that may be affected by sporadic RFI. The majority of these are at the edges of frequency ranges masked in Fig. 10. An updated RFI mask would get rid of them. This will certainly be the preferred strategy for defining frequency ranges to be used for continuum imaging. Here, we rejected all the absorption candidates that are within one frequency channel

Table 3. High probability 21-cm absorption candidates

Source name	z_{em}	$z_{abs}(21\text{-cm})$	$\int \tau dv(21\text{-cm})$	ΔV_{90}
			(km s^{-1})	(km s^{-1})
(1)	(2)	(3)	(4)	(5)
M0513+0100	2.673	1.9526	3.59 ± 0.67	107
M0618-3158	2.134	1.9642	0.49 ± 0.07	15
M1244-0446	3.114	2.3871	1.61 ± 0.27	70
M1312-2026	5.064	3.0324	0.34 ± 0.08	20
M1540-1453	2.098	2.1139	9.14 ± 0.28	144

NOTE— Column 1: source name. Column 2: emission redshift. Columns 3-5: HI 21-cm absorption redshift, integrated 21-cm optical depth limit and velocity width of absorption profile based on the survey spectra presented in Fig. 9, respectively. The spectra have been normalized using the corresponding peak flux densities.

of any of these false detections. This step reduced the number of absorption candidates by a factor of ~ 10 .

We visually examined RR and LL spectra of the remaining 48 absorption candidates for consistency. Specifically, we imposed the criteria that integrated optical depths estimated using the RR and LL spectra match within 3σ and within errors the absorption profiles appear similar.

After all the statistical filtering described above, we were left with a total of 15 candidates towards the sight lines which are identified in column 12 of Table 1. We extracted Stokes- I spectra of gain calibrators corresponding to these. For the following candidates: M0212-3822 ($z_{abs}=2.1666$), M0250-2627 ($z_{abs}=2.1665$), M0422-2034 ($z_{abs}=2.5924$), M0513+0100 ($z_{abs}=2.1612$, 2.3183, 2.6434), M0515-0120 ($z_{abs}=2.1753$), M0702-3302 ($z_{abs}=2.2769$), M1448-1122 ($z_{abs}=2.2973$) and M2017-2933 ($z_{abs}=2.0733$), we find an ‘absorption’ feature at the same redshifted frequency in the gain calibra-

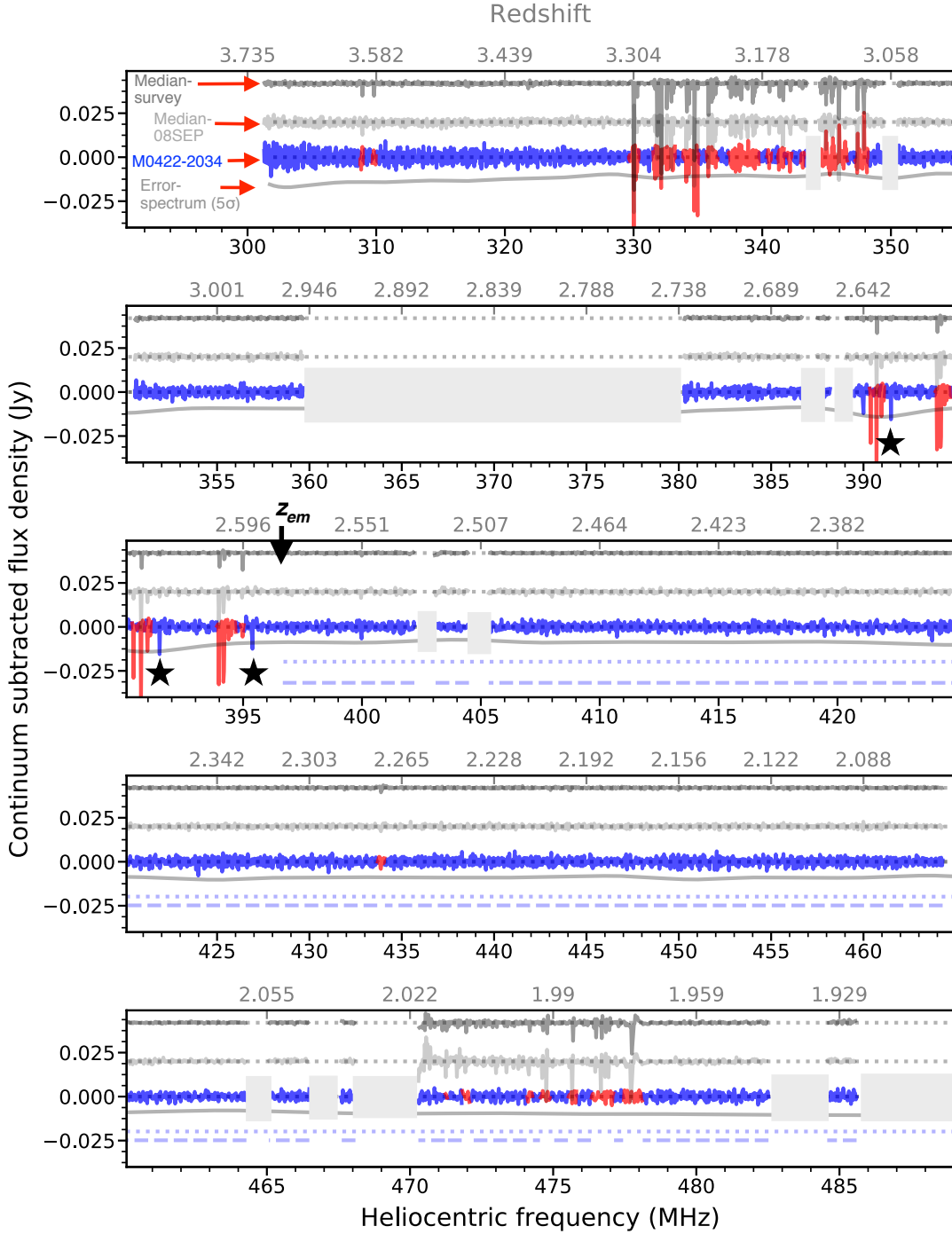


Figure 6. The continuum subtracted Stokes- I spectrum of M0422-2034 ($z_{em}=2.582$; see arrow at 396.51 MHz marking the redshifted H I 21-cm line frequency). Shaded regions mark frequency ranges that were masked prior to any calibration. The median spectra obtained using the full survey and only 08SEP run are plotted at +0.042 (median-survey) and +0.020 Jy (median-08SEP), respectively. In the spectrum of M0422-2034, the pixels flagged on the basis of median spectra are shown in red. The error spectrum ($5\times\sigma_{\text{rolling}}$) is also shown. The dotted and dashed lines at the bottom in panels 3-5 show the frequency range valid for 21-cm line search and actually contributing to the sensitivity function ($g(z)$), respectively. The candidate detections are marked using \star .

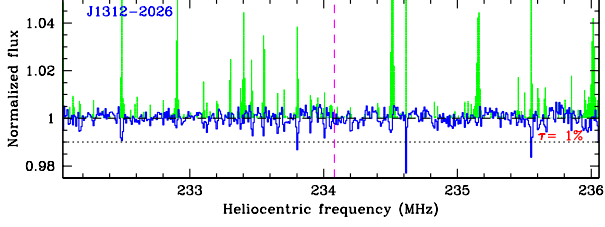


Figure 7. H I 21-cm absorption spectrum towards the highest redshift quasar M1312-2026 in our sample. The vertical dashed line marks the redshifted H I 21-cm absorption frequency corresponding to z_q . The filled histogram in the background is the ratio of the extent of the absorption to the extent of the data flagged due to frequency-dependent and frequency-independent flags.

tor spectrum. The angular separation between a target source and its gain calibrator is typically 15 degree. Thus, it is unrealistic that at $z > 2$ a true absorption is present in both of them. Therefore we rejected these 10 candidates.

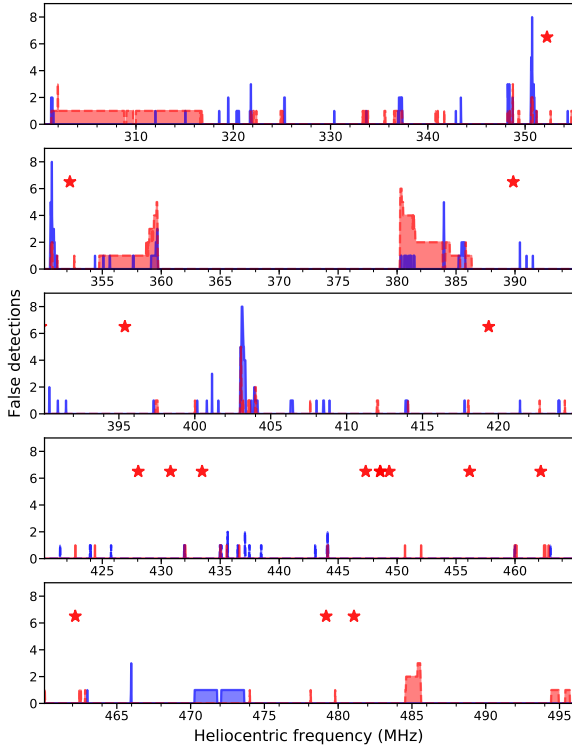


Figure 8. Distribution of false absorption (blue) and emission (red) detections for the survey. The majority of these are the edges of frequency regions masked in Fig. 10. The locations of absorption candidates (see column 12 of Table 1) are marked by \star .

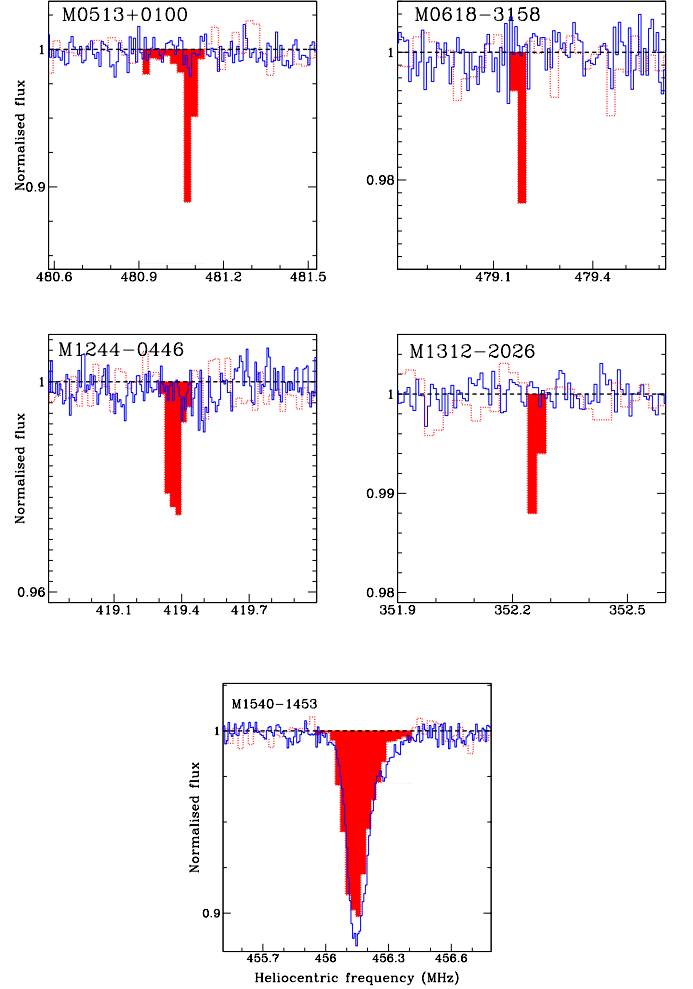


Figure 9. High probability absorption candidates. The survey and reobservation spectra are shown as dotted (red) and solid (blue) lines, respectively.

Finally, we have 5 high probability candidates. These are listed in Table 3. We also estimated integrated optical depths ($\int \tau dv$) and velocity width (ΔV_{90}) corresponding to the 5% and 95% percentiles of the apparent optical depth distribution. These are very similar to the values observed for 21-cm absorption lines detected in various surveys (see e.g., Gupta et al. 2009; Dutta et al. 2017c).

We reobserved these high probability candidates with uGMRT (see Section 3.1 and Table 2) using a bandwidth of 6.25 MHz centered at H I 21-cm line frequency corresponding to $z_{abs}(21\text{-cm})$ given in column 3 of Table 3. These observations were carried out at night to reduce the effect of RFI. For better RFI mitigation, the frequency setup was chosen to provide a spectral resolution of $\sim 1 \text{ km s}^{-1}$. Recall, the survey observations had a spectral resolution of $\sim 18 \text{ km s}^{-1}$. In Fig. 9, we

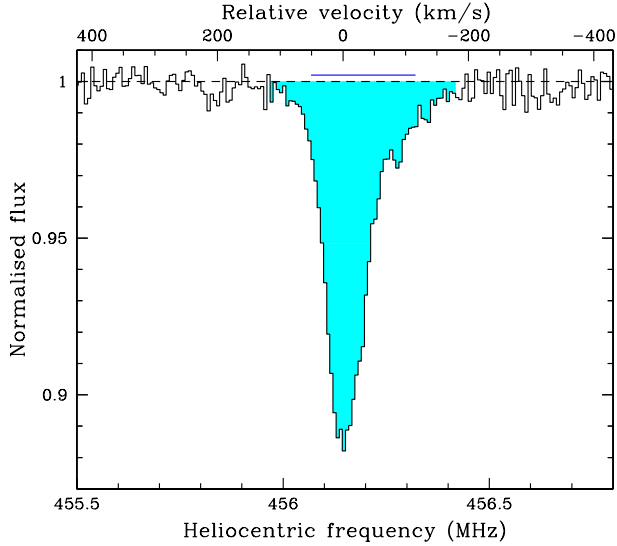


Figure 10. Associated H I 21-cm absorption detection towards M1540-1453. The zero of the velocity scale is defined with respect to the peak of the absorption i.e., $z_{\text{abs}} = 2.1139$. The solid horizontal line corresponds to ΔV_{90} .

present profiles from the survey and reobservation spectra. Clearly, only M1540-1453 is confirmed. The remaining 4 candidates are due to RFI.

To summarize, based purely on the uGMRT survey spectra and blind 21-cm line search, we identified 5 absorption features (4 intervening and 1 associated systems). The followup observations confirmed only one of these i.e., absorption associated with the radio source M1540-1453 at $z_{\text{em}} = 2.098$. The distribution of 5σ 21-cm optical depth limits at 420 MHz estimated assuming $\Delta v = 25 \text{ km s}^{-1}$ is shown in Fig. 4. The median 0.535 km s^{-1} is well below the sensitivity (1.1 km s^{-1}) required to detect CNM (i.e. $T \sim 100 \text{ K}$) in DLAs (i.e. $N(\text{H I}) \geq 10^{20.3} \text{ cm}^{-2}$).

4. ASSOCIATED H I 21-CM ABSORPTION DETECTION TOWARDS M1540-1453

The H I 21-cm absorption spectrum of M1540-1453 based on the followup observation is presented in Fig. 10. It is normalized using the corresponding peak continuum flux density of $652 \text{ mJy beam}^{-1}$. The absorption is spread over $\sim 300 \text{ km s}^{-1}$. We measure a total optical depth, $\int \tau dv = 11.30 \pm 0.07 \text{ km s}^{-1}$ and about 90% of this is confined to $\Delta V_{90} = 167 \text{ km s}^{-1}$. This translates to a H I column density of $(2.06 \pm 0.01) \times 10^{21} \left(\frac{T_s}{100}\right) \left(\frac{1}{f_c}\right) \text{ cm}^{-2}$. Here, T_s is the spin temperature in Kelvin and f_c is covering factor of absorbing gas. We note that measuring the covering factor of the absorbing gas would require milliarcsecond scale spectroscopy which is currently not

feasible at $z > 0.2$ (Srianand et al. 2013; Gupta et al. 2018b). Therefore, unless explicitly stated otherwise, hereafter, we will assume $f_c = 1$. We also assume $T_s = 100 \text{ K}$ for the CNM (Heiles & Troland 2003).

We obtained an optical spectrum of M1540-1453 using the Robert Stobie Spectrograph (RSS; Burgh et al. 2003; Kobulnicky et al. 2003) on SALT as part of our optical survey summarized in Section 2. The spectrum has a typical signal-to-noise ratio (SNR) of 7 per pixel. It shows C IV and [C III] emission lines. The spectral SNR close to the [C III] emission line is poor due to residuals from the subtraction of skylines. Hence, we focus on the C IV emission line. The peak of C IV emission corresponds to $z_{\text{em}} \simeq 2.113$ which is consistent with the 21-cm absorption peak (Fig. 10). The emission line is superimposed with absorption lines possibly also of C IV but at a redshift slightly lower than the 21-cm absorption.

Our SALT spectrum does not cover Ly α absorption for M1540-1453. But it covers the rest wavelength range of 1436 to 2414 Å. Although the region is affected by skylines, in principle, we have access to the Fe II lines associated with the 21-cm absorption. We detect an absorption feature exactly at the redshifted wavelength corresponding to Fe II $\lambda 2383$ line. The redshift and rest equivalent width of the absorption are $z_{\text{abs}} = 2.11404$ and $W_r = 1.05 \pm 0.25 \text{ Å}$, respectively. We also find absorption dips at the expected positions of the Fe II $\lambda 2344$, Fe II $\lambda 2374$ and Si II $\lambda 1526$ lines. These coincidences are interesting because metal absorption line ratios can be a reasonable indicator of H I column density (Rao et al. 2006; Gupta et al. 2012; Dutta et al. 2017b). We note that the rest frame ultraviolet luminosity of the quasar at 912 Å i.e., $L_{912} = 1.4 \times 10^{23} \text{ W Hz}^{-1}$ (see Section 6 for details). This is marginally above the ultraviolet cutoff of $10^{23} \text{ W Hz}^{-1}$ above which H I 21-cm absorption is rarely detected (Curran & Whiting 2010). A better quality optical spectrum covering Ly α and above-mentioned metal lines is needed to extract physical conditions prevailing in the absorbing gas.

We follow the method described in Srianand et al. (2008) to constrain the visual extinction, A_V . Using our flux calibrated SALT spectrum along with the Small Magellanic Cloud (SMC) type extinction curve and the average QSO spectral energy distribution (SED) given in Selsing et al. (2016), we measure, $A_V = 0.13 \pm 0.01$. The moderate extinction observed towards M1540-1453 is consistent with the idea that cold atomic gas is accompanied by dust (see Fig. 9 of Dutta et al. 2017b).

To date only three associated HI 21-cm absorbers are known² at $z > 2$. These are: $z_{\text{abs}} = 3.3968$ towards B2 0902+345 (Uson et al. 1991; Briggs et al. 1993), $z_{\text{abs}} = 2.6365$ towards MG J0414+0534 (Moore et al. 1999) and $z_{\text{abs}} = 3.52965$ towards 8C 0604+728 (Aditya et al. 2021). Thus, M1540-1453 absorber reported here is only the fourth detection at $z > 2$. The inferred column densities for reasonably assumed values of spin temperature and covering factor ($T_s = 100$ K; $f_c = 1$) imply $N(\text{HI}) \gg 2 \times 10^{20} \text{ cm}^{-2}$ which is the formal DLA cut-off. So, in all these cases if the optical and radio sightlines coincide then one expects to see a DLA at the 21-cm absorption redshift. We investigate this for B2 0902+345 and MG J0414+0534, the two sources for which optical spectra are available in literature.

B2 0902+345 is associated with a radio galaxy that exhibits Ly α emission extended up to 50 kpc. The associated radio continuum emission ($\alpha = -0.94$) has a highly distorted radio morphology over $6''$ (~ 45 kpc at z_{abs}) and rotation measure in excess of 1000 rad m^{-2} (Carilli et al. 1994). However, no signatures of Ly α absorption associated with the 21-cm absorber are seen. In fact, the 21-cm absorption is found to be redshifted with respect to the Ly α emission (shift $\sim +300 \text{ km s}^{-1}$; see Adams et al. 2009, for details).

MG J0414+0534 is a highly reddened gravitationally lensed quasar ($A_V \sim 5$ Lawrence et al. 1995b). The weakness of Ly α emission prevents us from searching for a DLA. However 4 associated strong Fe II absorption components are detected in the redshift range 2.6317-2.6447 (Lawrence et al. 1995a). These are within the range over which CO emission is detected but do not exactly coincide with the 21-cm absorption redshift, which itself is shifted by $\sim 200 \text{ km s}^{-1}$ with respect to the peak of the CO emission line. The 21-cm absorption in this case may actually be towards a steep-spectrum radio jet component not spatially coinciding with the AGN (Moore et al. 1999). The same scenario may also apply to B2 0902+345.

In comparison, the radio emission associated with M1540-1453 is compact in VLASS and the radio continuum peak coincides well with the PS1/MIR counterparts. The deconvolved radio source size is $1.8'' \times 0.7''$ with a position angle of 155° . This corresponds to an upper limit on the size of ~ 10 kpc at $z_{\text{abs}} = 2.1139$. Clearly, milliarcsecond scale imaging is required to esti-

mate f_c and understand the coincidence between 21-cm absorption and metal absorption lines observed towards this source. Interestingly, the HI 21-cm absorption is only slightly asymmetric at the base and does not show signatures of outflows i.e., blue-shifted absorption (Vermeulen et al. 2003; Gupta et al. 2006). In low- z samples, such absorption likely originates from the circumnuclear disk or gas clouds associated with the host galaxy (e.g., Geréb et al. 2015; Srianand et al. 2015). In Section 6, we note that the quasars in our sample are generally hosted in gas and dust poor galaxies. The CO emission line and millimetre continuum observations of M1540-1453 will reveal the nature of its host galaxy ISM and shed light on the origin of gas detected in 21-cm absorption.

5. INTERVENING ABSORPTION STATISTICS

In this section, we constrain the occurrence of intervening HI 21-cm absorbers at $z > 2$ using a blind spectroscopic search. We also use Ly α and metal absorption lines detected in our SALT spectra to interpret these statistics.

5.1. Blind HI 21-cm absorption line search

To estimate the incidence of intervening absorbers, we first determine the sensitivity function, $g(\mathcal{T}, z)$, as a function of integrated optical depth (\mathcal{T}) and redshift (z). For this we follow the formalism provided in Gupta et al. (2021) which takes into account the varying optical depth sensitivity across the spectrum. The two crucial inputs required to determine $g(\mathcal{T}, z)$ are spectral weight (W) and completeness fraction (C). The former accounts for the possibility that some of the targets in the sample may not have spectroscopic redshifts. Since, all the targets in our sample have spectroscopic redshifts, we assign $W = 1$.

The completeness fraction accounts for the detectability of absorption line features of different line shapes. To determine this we consider the absorption profiles of all the intervening absorbers detected from our surveys in last 15 years. We inject 200 single Gaussian components with widths consistent with the distribution of ΔV_{90} of these absorbers (see Fig. 8 of Gupta et al. 2021) at each pixel and apply the detection algorithm described in Section 3.3 to compute $C(\mathcal{T}_j, z_k)$ as

$$C(\mathcal{T}_j, z_k) = \frac{1}{N_{inj}} \sum_{i=1}^{N_{inj}} F(\mathcal{T}_j, z_k, \Delta V_i), \quad (2)$$

where N_{inj} is the number of injected systems and $F = 1$ if the injected system is detected and 0 if not. The total completeness corrected redshift path of the survey,

² We note that HI 21-cm absorber ($z_{\text{abs}} = 1.9436$) has been detected towards the QSO PKS 1157+014 at $z_{\text{em}} = 1.978$ (Wolfe et al. 1981) which is slightly below the redshift cut-off used here. It is suggested that in this case the absorption originates from a galaxy bound to the cluster containing the QSO.

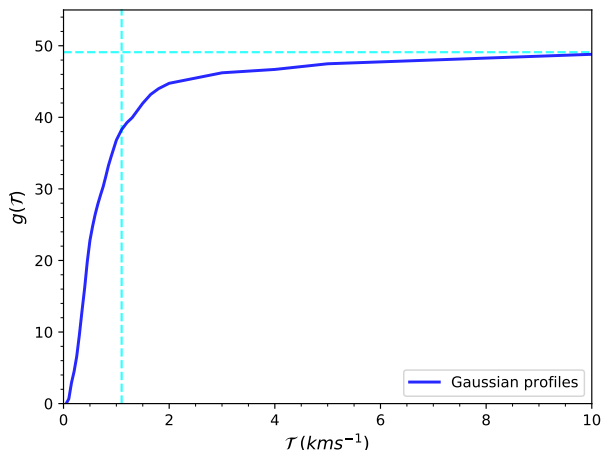


Figure 11. Completeness corrected total redshift paths ($\Delta z(\mathcal{T}) \equiv g(\mathcal{T})$) for the 21-cm line search. The horizontal dashed line represents total redshift path without completeness correction. The vertical dashed lines correspond to integrated optical depth, $\mathcal{T} = 1.1 \text{ km s}^{-1}$. This corresponds to a 5σ detection limit of $N(\text{H I}) = 2 \times 10^{20} \text{ cm}^{-2}$ for $T_s = 100 \text{ K}$.

$g(\mathcal{T}_j)$, considering all sight lines is plotted in Fig. 11. The redshift path starts falling off rapidly below $\mathcal{T} = 1.5 \text{ km s}^{-1}$.

It is of particular interest to consider the detectability of H I 21-cm absorption in DLAs, i.e., $\mathcal{T} = 1.1 \text{ km s}^{-1}$ (refer to vertical dashed line in Fig. 11). The sensitivity function providing the number of spectra in which it is possible to detect CNM in DLAs is shown in Fig. 12. The total redshift and comoving path length are $\Delta z = 38.3$ and $\Delta X = 130.1$, respectively. Then, the incidence or number of 21-cm absorbers per unit redshift and comoving path length are $n_{21} < 0.048$ and $\ell_{21} < 0.014$, respectively. These 1σ upper limits are based on small number Poisson statistics (Gehrels 1986).

The formalism to search for H I 21-cm absorption line presented above can also be applied to OH main lines. For stronger OH main line at 1667.359 MHz, $\mathcal{T} = 1.1 \text{ km s}^{-1}$ and excitation temperature of 3.5 K will correspond to $N(\text{OH}) = 8.6 \times 10^{14} \text{ cm}^{-2}$. The total redshift and comoving path length are $\Delta z = 44.9$ and $\Delta X = 167.7$, respectively. The number of OH absorbers per unit redshift and comoving path length are $n_{\text{OH}} = 0.041$ and $\ell_{\text{OH}} < 0.011$, respectively.

Besides H I 21-cm absorption, CNM at high- z may also be searched using absorption lines of H_2 and C I (e.g., Srianand et al. 2012; Noterdaeme et al. 2018). Recently, Krogager & Noterdaeme (2020) using a canonical two phase model of atomic gas and the observed statistics of H_2 and C I absorbers at high- z estimated the comoving path length of CNM, $n_{\text{CNM}} = 0.012$. The

upper limit of $n_{21} < 0.048$ obtained through our blind survey is consistent with this. This result is the first study comparing the CNM cross-section of galaxies at $z > 2$ estimated using radio and optical/ultraviolet absorption lines. The detectability of H_2 and C I absorption at optical/ultraviolet and H I 21-cm absorption at radio wavelength are affected by different systematic effects. Indeed, there does not exist a one-to-one correspondence between the presence of H_2 and H I 21-cm absorption, and the difference may be due to small sizes of H_2 bearing clouds (see Srianand et al. 2012, for a discussion). Much larger radio surveys are needed to disentangle these possibilities.

5.2. Relationship with Ly α and metal lines

Our SALT spectra allow us to search for Fe II $\lambda\lambda\lambda 2343, 2374, 2383$ for $z_{\text{abs}} \leq 2.15$ and DLAs at $z > 2.65$. For this search, we complement our SALT-NOT survey spectra with more sensitive long-slit SALT observations of 25 quasars $z_{\text{em}} > 2.7$ obtained to search for extended Ly α emission halos associated with powerful radio loud quasars (see Shukla et al. 2021, for an example). In total, we identify 7 DLAs and 1 strong Fe II absorber in our sample. Implications of lack of 21-cm absorption in these high H I column density absorbers are discussed below. In the redshift range $2.15 \leq z_{\text{abs}} \leq 2.65$ we also identify 21 C IV absorbers for which neither Fe II nor DLA can be searched in our spectrum. The redshifted H I 21-cm line frequencies corresponding to these C IV absorbers are unaffected by RFI and no H I absorption is detected. Note that C IV can trace a wide range of ionization stages and so is not a good indicator of the presence of a DLA or 21-cm absorption. We will use this only as an indicator of the possible presence of multi-phase gas along the sight line.

First, we focus on the subset of 23 quasars that have sufficient SNR in optical continuum and, hence, suitable to search for Ly α absorption. The absorption profiles of 6 DLAs detected from this subsample are shown in Fig. 13. The measured absorption redshifts are consistent with 5 of these being intervening systems and remaining one ($z_{\text{abs}} = 2.7613$ towards M2154-3826) being a PDLA.

We also detect strong Ly α absorption at the systemic redshift of M0507-3624. While we see the evidence of the damping wings and a wide range of absorption from singly ionised species, we also see non-zero flux in the core of the Ly α absorption line. It is possible that this system is similar to the associated H_2 bearing DLAs studied by Noterdaeme et al. (2019) where the presence of flux in the absorption core is related to the partial coverage. Based on damping wings we estimate

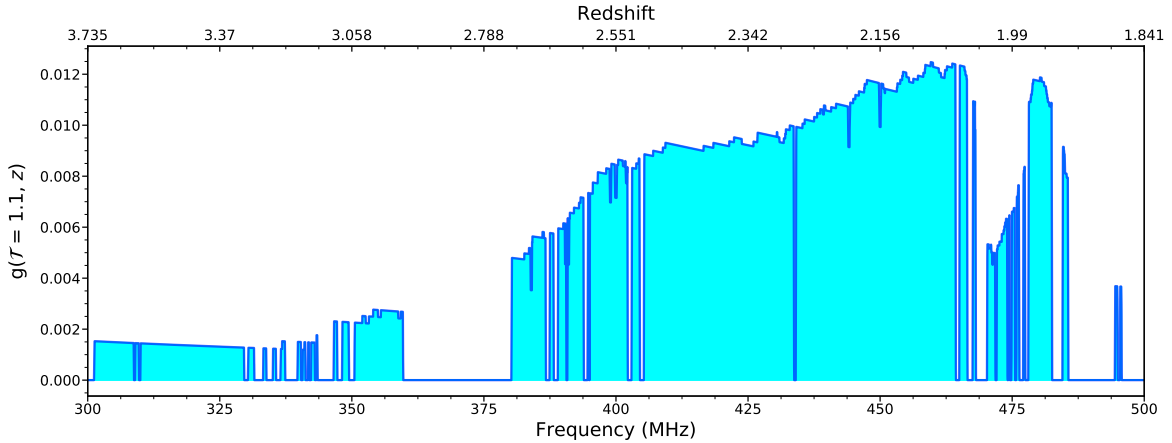


Figure 12. The sensitivity function, $g(z)$, for HI 21-cm absorbers with integrated 21-cm optical depth $\mathcal{T} \geq 1.1 \text{ km s}^{-1}$. The abrupt dips are caused by the spectral channels removed from the data due to RFI. Approximately 30% of the redshift path is lost due to RFI.

Table 4. Properties of the DLAs derived from our observations

QSO	z_{abs}	$\log N(\text{H I})$	$W(\text{Si II})$	$Z(\text{P08})$	Z	$\int \tau_{21} dv$	T_s
			(\AA)			(km s^{-1})	(K)
(1)	(2)	(3)	(4)	(5)	(6)	(7)	(8)
M0416-3339	2.8561	20.50 ± 0.10	0.12 ± 0.03	-2.2	$\leq -2.3^a$	RFI
M0610-2301	2.3987	20.85 ± 0.10	0.66 ± 0.02	-1.2	$\leq -1.1^b$	≤ 0.64	≥ 603
M1013-2546	2.6834	20.35 ± 0.15	≤ 0.90	≤ 0.72	≥ 169
M1351-0129	2.7719	20.50 ± 0.10	0.19 ± 0.03	-1.9	$\leq -1.2^c$	RFI
M1619-0939	2.7934	20.55 ± 0.10	1.03 ± 0.05	-0.9	$\leq -1.9^c$	RFI
M2154-3826	2.7613	21.00 ± 0.10	0.53 ± 0.01	-1.3	-1.60 ± 0.11^d

NOTE— Column 1: source name. Columns 2 and 3: DLA redshift and HI column density. Column 4: Si II equivalent width. Column 5: metallicity inferred using $W(\text{Si II})$ and correlation from Prochaska et al. (2008a). Column 6: metallicity measured using weak Si II or S I lines. Column 7: 5σ 21-cm optical depth limit, considering $\Delta v = 25 \text{ km s}^{-1}$.
 a : Based on Si II $\lambda 1301$ line; b : Based on S II $\lambda 1250$ line; c : Based on Si II $\lambda 1808$ line; d : Using the curve of growth analysis.

$N(\text{H I}) \sim 10^{20.2} \text{ cm}^{-2}$. However, with the present spectra we are unable to confirm the origin of residual flux in the core. Higher spectral resolution dataset covering both Ly α and Ly β absorption is needed to get an accurate estimate of the $N(\text{H I})$ for this absorber. For the purpose of this paper, we consider this as a candidate PDLA.

For a total redshift path of 9.3, the detection of 5 intervening DLAs correspond to a number of DLAs per unit redshift, $n_{\text{DLA}} = 0.54 \pm 0.24$. This is slightly higher but due to large uncertainties consistent with the measurement of 0.24 ± 0.02 based on SDSS DLAs by Noterdaeme et al. (2012), and $0.26^{+0.06}_{-0.05}$ towards radio-loud quasars based on the combined CORALS and UCSD samples by

Jorgenson et al. (2006). Since, the quasars in our sample are fainter than previous surveys (see Fig. 1), it is also possible that there is indeed a dependence between n_{DLA} and the faintness of quasars as noted by Ellison et al. (2001) for the CORALS sample.

As discussed in next section, in comparison to associated HI 21-cm absorption detection rates in low- z AGNs, the detection of just 2 PDLAs and one associated HI 21-cm absorber (M1540-1453) from our sample may seem surprisingly low. But actually the detection of 3 PDLAs from our sample is in fact a factor of 3 larger than what we expect from the statistics of PDLAs observed at $z \sim 3$ in SDSS (Prochaska et al. 2008a). Interestingly, from the statistics of damped H₂ absorption

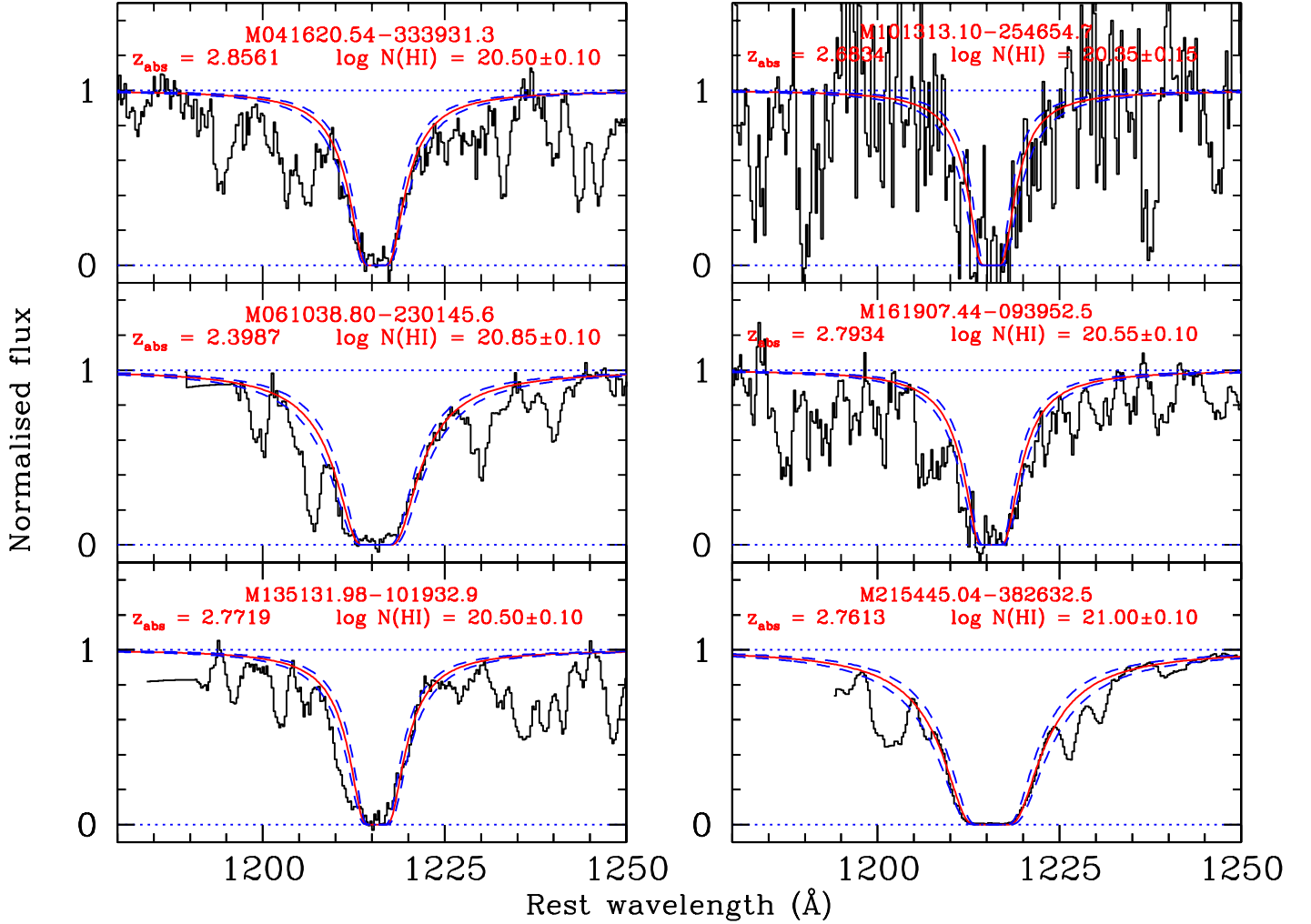


Figure 13. Voigt profile fits to the 6 DLAs detected in our new radio loud quasar sample. The profiles given in solid and long-dashed lines correspond to the best fit and 1σ range around it respectively. The absorption redshift and the best fit $N(\text{H I})$ obtained are also provided in each panel.

lines, [Noterdaeme et al. \(2019\)](#) have suggested that the PDLA fraction in [Prochaska et al. \(2008b\)](#) may have been underestimated. A complete search of Ly α absorption towards all the targets in our sample will confirm the above mentioned excesses of DLAs and PDLAs. Specifically, from the observations of all the sources ($\Delta z \sim 60$), we expect to detect another ~ 30 DLAs.

Using SALT 1D spectra we measure redshift, $N(\text{H I})$ and rest equivalent widths of metal absorption lines corresponding to these DLAs. These measurements are provided in Table. 4. The quoted error in $N(\text{H I})$ also include continuum placement uncertainties. The single component Voigt profile fits to the DLAs are shown in Fig 13. The rest equivalent width of Si II $\lambda 1526\text{\AA}$ lines are provided in column 4 of Table. 4. The metallicities

inferred using the W(Si II) and metallicity correlation (see equation 1 of [Prochaska et al. 2008a](#)) are given in column 5. We also estimated metallicity using weak transitions of Si II or S II. These are provided in column 6. For $z_{\text{abs}} = 2.7613$ PDLA towards M2154–3826 we detect several weak transitions of Fe II, Ni II and Si II. We used single component curve of growth to measure metallicities in this case. Overall, the metallicities of these DLAs are typically less than a tenth of the solar metallicity. However, given the poor spectral resolution of our data these estimates may suffer from hidden saturation effects.

Unfortunately strong persistent RFI at 360-380 MHz prevents HI 21-cm line search at $z = 2.73$ -2.94 (see Fig. 12). Thus, we could observe 21-cm line only for

the $z_{\text{abs}} = 2.3987$ DLA towards M0610-2301 and $z_{\text{abs}} = 2.6834$ towards M1013-2546. We do not detect 21-cm absorption from these systems. The 5σ integrated optical depths are provided in column 7 of Table 4. M0610-2301 is a compact radio source in the modest quality VLASS quick look image. The deconvolved source size is $1.3'' \times 0.1''$ with a position angle of 180° (i.e., size < 11 kpc at z_{abs}). M1013-2546 also appears to be a core-dominated source. Thus, we assume complete coverage i.e., $f_c = 1$. This together with the observed $N(\text{H I})$ translates to a lower limit on the spin temperature, $T_S \geq 603$ K for M0610-2301 and ≥ 169 K for M1013-2546. These limiting values of spin temperatures are higher than the measured median $N(\text{H I})$ weighted T_S of 70 K for the cold neutral medium (CNM) in our galaxy (see Heiles & Troland 2003). We note that H I 21-cm observations of 23 DLAs from radio-selected samples of CORALS, UCSD and Ellison et al. (2008) are available in the literature (Srianand et al. 2012; Kanekar et al. 2014). The overall 21-cm absorption detection rate of $3/25$ ($12^{+11}_{-7}\%$) is consistent with the measurements from optically selected samples and the conclusion that DLAs at $z > 2$ are predominantly warm and tend to show high spin temperatures (see also Petitjean et al. 2000). Much larger radio-selected surveys ($\Delta X \gtrsim 10^4$) are needed to uncover the population of dusty DLAs.

Our SALT spectra also allow us to detect Fe II $\lambda 2383$ line for $z_{\text{abs}} \leq 2.15$. We detect a strong Fe II absorber at $z_{\text{abs}} = 2.1404$ towards M0652-3230. This system also shows absorption lines from other singly ionized species (i.e Si II and Al II). All these suggest high $N(\text{H I})$ (Dutta et al. 2017b). But as can be seen from Fig. 3, the radio emission is dominated by the double lobe structure. The separation between the two lobes is $\sim 27''$ (250 kpc at z_{abs}). Therefore, the radio and optical sight lines are well separated. This explains the non-detection of 21-cm absorption at the redshift of Fe II absorbers.

6. ASSOCIATED ABSORPTION STATISTICS

We searched for H I 21-cm absorption within 3000 km s^{-1} to the quasar emission line redshift. In 28/88 cases (32%), the redshifted frequency is affected by RFI. For remaining 60 sources, the distributions of redshift and 5σ 21-cm optical depth limit for a width of 25 km s^{-1} are shown in Fig. 14. The median redshift of this subsample which includes M1312-2026 ($z = 5.064$) is 2.288. For sources with resolved morphology (Fig. 3), we have searched for absorption towards multiple components but consider only the optical depth limit for the strongest component for statistics.

The only 21-cm absorption detection from the survey is described in Section 4. For non-detections, the opti-

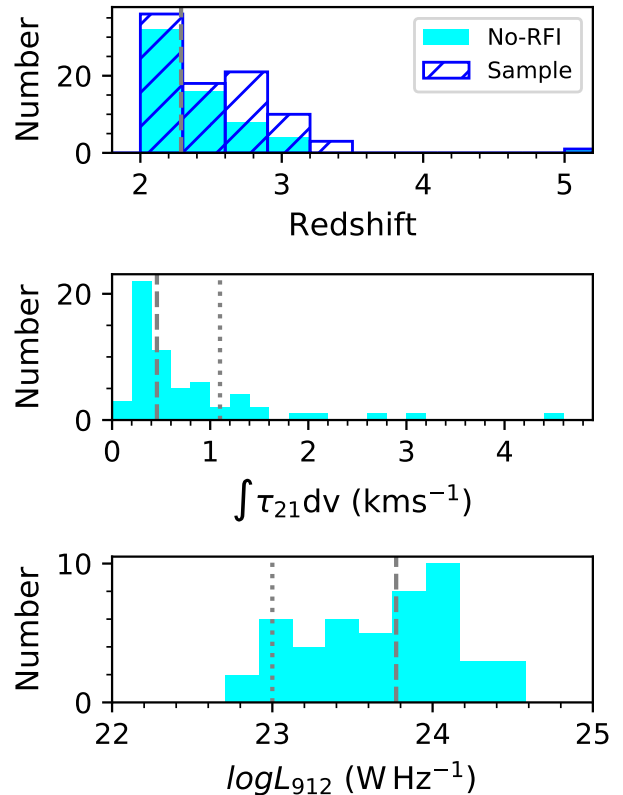


Figure 14. Distributions of quasar redshift (hatched histogram for all targets and filled for those unaffected by RFI), 5σ 21-cm optical depth limits and 912\AA luminosities for the AGNs searched for associated H I absorption. The vertical dashed lines mark the median for each distribution. The dotted lines in middle and bottom panels correspond to $\int \tau_{21} dv = 1.1 \text{ km s}^{-1}$ and $L_{912} = 10^{23} \text{ W Hz}^{-1}$.

cal depth limits span a range of $0.103 - 3.6 \text{ km s}^{-1}$. The detection rate of $1.6^{+3.8}_{-1.4}\%$ without any sensitivity cut is among the lowest for a 21-cm absorption line survey. If we adopt the detection rate based on low- z surveys, we would expect to detect approximately 20 H I 21-cm absorbers from our sample. For example, Maccagni et al. (2017) reported a $27\% \pm 5\%$ detection rate from the observations of 248 AGNs at $0.02 < z < 0.25$. The 3σ peak optical depth (resolution $\sim 16 \text{ km s}^{-1}$) limits are typically between 0.005 - 0.2 (median ~ 0.04). For 25 km s^{-1} width adopted by us, the range corresponds to 5σ integrated optical depth, \mathcal{T} , of 0.2 - 7.1 km s^{-1} (median ~ 1.41). In our survey, we achieve \mathcal{T} better than 1.1 km s^{-1} in 90% of the cases. Thus, stark contrast in detection rates is not due to differences in the sensitivity.

At low- z , the vast majority of targets have WISE color $W1 - W2$, which is an indicator of AGN accretion rate, to be less than 0.6. Among these the higher fraction of detections are associated with larger $W2 - W3$ colors, which is an indicator of star formation rate (Glowacki

et al. 2017; Chandola et al. 2020). The compact radio sources still embedded within such gas and dust rich environments are well placed to exhibit 21-cm detections. The powerful quasars identified by our MIR-wedge (see equation 1) do not overlap with the above-mentioned low- z AGNs in color space defined by $W1 - W2$ and $W2 - W3$. Thus, we hypothesize that the low non-detection rate in our sample is a consequence of the gas poor environment of host galaxies. Since the detectability of HI 21-cm absorption also depends on the thermal state of the gas and the morphology of radio emission, we validate this hypothesis through Ly α and metal lines covered in our SALT-NOT spectra.

First, we consider following four sources³ at $2.7 < z < 3.5$: M0507–3624, M1013–2546, M1351–1019 and M2047–1841. For these we have access to both Ly α and metal absorption lines and the 21-cm frequency is not affected by RFI. In the cases of M1013–2546 and M2047–1841, we do not detect a PDLA or any associated CIV absorption system. This suggests the absence of neutral and metal enriched ionized gas along the sight lines. In the case of M0507–3624, we identified a potential PDLA. For $N(\text{H I}) \sim 10^{20.2} \text{ cm}^{-2}$ inferred from the damping wing of Ly α absorption and HI 21-cm non-detection, we place a lower limit of 216 K for the spin temperature ($f_c = 1$). In the case of M1351–1019 while Ly α absorption is not prominent we do detect associated CIV absorption. In this case, we also detect extended Ly α emission. All this suggests that these two sources are associated with gas rich environment. Therefore, the lack of HI 21-cm absorption here may just be due to lower CNM filling factor.

In general, 22 i.e., $\sim 23\%$ quasars in our sample show associated CIV absorption within 3000 km s^{-1} to the z_{em} . In 11 of these cases 21-cm absorption could not be searched due to strong RFI. Among remaining 10, we also detect HI Ly α absorption in 4 cases but none are DLAs. In the remaining 6 cases, the Ly α absorption is not covered in the spectra but we do not detect corresponding absorption due to any low-ionization species such as Fe II (in 4 cases) and Si II (in 6 cases). Since CIV may come from a wide range of ionization stages, the absence of strong Ly α and low-ionization absorption lines indicate the lack of sufficient high column density neutral gas along the line of sight.

From the above we conclude that the high fraction of quasars in our sample are indeed residing in gas and dust poor environments. An interesting counterpoint to the lack of HI 21-cm absorption in our sam-

ple is provided by the 100% detection rate of molecular gas through CO emission in a sample of eight hyper-luminous WISE/SDSS (WISSH) quasars at $z \sim 2 - 4$ (Bischetti et al. 2021). We note that a majority (6/8) of these would be selected by our MIR-wedge (Equation 1). But WISSH quasars are much brighter (1.5 Vega magnitude compared to our sample) in the $W4$ band ($22\mu\text{m}$) of WISE. The deliberate selection of WISSH quasars as most luminous infrared sources ensures that they are being observed through dust clouds (Weedman et al. 2012), and perhaps represent an early phase in the evolution of quasar. Approximately only $\sim 10\%$ of quasars in our sample have $W4$ magnitudes comparable to above-mentioned WISSH quasars with CO detections, and only in 3 cases $\mathcal{T} < 1.1 \text{ km s}^{-1}$ i.e., the sensitivity to detect CNM in $N(\text{H I}) > 10^{20} \text{ cm}^{-2}$ is achieved. Although this may seem to conflict with our MIR-selected sample strategy but luminous quasars only spend a small fraction of their total lifetime ($\sim 10^7 \text{ yr}$; Martini & Weinberg 2001) in the dust-obscured phase. Therefore, the the representation of dust-obscured quasars in our unbiased sample will also be proportionately small. Considering only the AGNs with sensitivity to detect CNM in $N(\text{H I}) > 10^{20} \text{ cm}^{-2}$ gas, we estimate the CNM covering factor in the unobscured phase of quasars with radio luminosity $L_{1.4 \text{ GHz}} \simeq 10^{27-29.3} \text{ W Hz}^{-1}$ to be 0.02.

Although, the most straightforward explanation for low detection rate in our sample is gas and dust poor environment at host galaxy scales but the detectability of gas towards the AGN may also be influenced by the additional factors such as high intrinsic radio or ultraviolet luminosities of AGN (Curran & Whiting 2010; Aditya et al. 2016; Grasha et al. 2019) and the distribution of gas at nuclear scales (Gupta & Saikia 2006). Since high L_{UV} merely helps to select core-dominated AGNs, these two are in fact interlinked in the context of AGN unification scheme. We estimate the 912\AA luminosities of the AGNs searched for associated HI 21-cm absorption by interpolating the photometry from PS1. The distribution of L_{912} is shown in the bottom panel of Fig. 14. Clearly, the majority of objects have $L_{912} > 10^{23} \text{ W Hz}^{-1}$, where the associated HI 21-cm absorption is rarely detected.

Unfortunately, none of the CO-detected quasars from Bischetti et al. (2021) are bright enough at radio wavelengths to search for HI 21-cm absorption. Interestingly, their available SDSS spectra do not show the presence of high-column density neutral gas i.e., a PDLA along the quasar sight line (although ionized gas outflows are present). Thus, although the molecular gas is distributed in rotating disks (extent 1.7 - 10 kpc; Bischetti et al. 2021), it is oriented such that cold gas cross-

³ We exclude M1312-2026 at $z = 5.064$ as all the lines except Ly α are redshifted into IR and not covered in our SALT spectrum.

section towards the quasar sight line is minimal. A spatially extended few kpc-sized radio source embedded in such an environment may have still shown HI 21-cm absorption (e.g., refer to the cases of B2 0902+345 and MG J0414+0534 in Section 4).

Finally, we note the non-detection towards the highest redshift quasar ($z_{\text{em}} = 5.062$) in our sample: M1312-2026 (see also Carilli et al. 2007, for 21-cm non-detections towards two $z \sim 5$ AGNs). This brightest radio loud quasar at $z > 5$, has a radio-loudness parameter of $R = f_{\nu, 5\text{GHz}}/f_{\nu, 4400\text{\AA}} = 1.4 \times 10^4$. This R value is an order-of-magnitude greater than that of any other $z > 5$ AGN known-to-date (Momjian et al. 2018; Saxena et al. 2018). The host galaxies of quasars at such high redshifts can be associated with large amounts of dust and molecular gas ($> 10^{10} M_{\odot}$), and high inferred star formation rates ($> 100 M_{\odot} \text{yr}^{-1}$) (Venemans et al. 2017; Decarli et al. 2018; Feruglio et al. 2018). Our HI 21-cm non-detection corresponds to a 5σ upper limit of $N(\text{HI}) < 4 \times 10^{19} \text{cm}^{-2} = 100 \text{K}$; $f_c = 1$ assumed) but can miss narrow absorption components due to the RFI. The current SALT spectrum also covers only Ly α emission. Further investigation on the nature of this very intriguing non-detection require IR spectra and sub-arcsecond scale radio imaging which are in progress.

7. SUMMARY AND OUTLOOK

This paper described a spectroscopically blind search for HI 21-cm absorption lines in the wide band uGMRT spectra of 88 AGNs at $2 < z < 5.1$. We also applied the same formalism to constrain the occurrence of intervening OH 18-cm main lines. We show that compared to previous radio-selected samples of quasars to search for DLAs, our sample for the uGMRT survey has targeted fainter objects (median $i = 19.5$ mag; see Fig. 2) and is a close representation of the underlying luminosity function of quasars. Thus, our dust-unbiased sample of AGNs with median radio spectral index, $\alpha_{0.4}^{1.4} = -0.38$, redshift, $z = 2.5$ and spectral luminosity, $L_{1.4\text{GHz}} = 10^{27-29.3} \text{WHz}^{-1}$ is ideally suited to determine the occurrence of cold atomic gas ($T \sim 100 \text{K}$) towards powerful quasars at $z > 2$.

Through a spectroscopically blind search of absorption lines in all the uGMRT spectra, we detected one new associated HI absorption which is towards M1540-1453 at $z_{\text{abs}} = 2.1139$. No intervening HI 21-cm absorption line is detected. Our detection is only the fourth associated HI 21-cm absorber known at $z > 2$. It has a HI column density of $(2.06 \pm 0.01) \times 10^{21} (\frac{T_s}{100}) (\frac{1}{f_c}) \text{cm}^{-2}$. In our SALT spectrum, the peak of CIV emission and low-ionization metal absorption lines are coincident with that of the 21-cm absorption. The over-

all properties of 21-cm absorption are consistent with it originating from a circumnuclear disk or gas clouds associated with the host galaxy. The CO emission line observations and optical spectra covering the Ly α absorption (i.e., $\lambda \sim 3785\text{\AA}$) along with the sub-arcsecond scale imaging will allow us to understand the origin of cold gas detected in 21-cm absorption.

Our survey is sensitive to detect CNM in DLAs corresponding to a total redshift and comoving path length of $\Delta z = 38.3$ and $\Delta X = 130.1$, respectively. Using this we constrain the incidence or number of 21-cm absorbers per unit redshift and comoving path length to be $n_{21} < 0.048$ and $\ell_{21} < 0.014$, respectively. The same formalism applied to OH main line at 1667.359 MHz corresponds to total redshift and comoving path length of $\Delta z = 44.9$ and $\Delta X = 167.7$, respectively. The number of OH absorbers per unit redshift and comoving path length are $n_{\text{OH}} < 0.041$ and $\ell_{\text{OH}} < 0.011$, respectively. We note that the number of DLAs per unit redshift interval i.e., $n_{\text{DLA}}(z)$ at $2.3 \leq z \leq 2.9$ is in the range of 0.21 to 0.29 (Noterdaeme et al. 2012). This implies that the covering factor of CNM gas in DLAs is ≤ 20 percent. These upper limits are also consistent with $n_{\text{CNM}} = 0.012$ estimated using H $_2$ and C I absorbers, also tracers of cold gas, at high- z (Krogager & Noterdaeme 2020). Our result shows that a moderately larger survey such as MALS with $\Delta X \gtrsim 10^4$ is important to precisely characterise the CNM fraction and its redshift evolution at high- z .

The low- z AGNs ($z < 0.25$) exhibit HI 21-cm absorption detection rates of $\sim 30\%$ (e.g., Maccagni et al. 2017). Compared to this the low associated HI 21-cm absorption detection rate ($1.6_{-1.4}^{+3.8}\%$) and the CNM filling factor of 0.2 from our survey is intriguing. We show that this is most likely due to the fact that the powerful quasars in our sample are residing in gas and dust poor environments, and that luminous quasars only spend a small fraction of their total lifetime in dust-obscured phase. We use the spectral coverage of Ly α and various metal absorption lines in our optical spectra to confirm the absence of high column density atomic gas towards the quasar sight lines.

From our SALT spectra, we report detections of 5 intervening DLAs and 2 PDLAs in our sample. The measured number of DLAs per unit redshift, $n_{\text{DLA}} = 0.54 \pm 0.24$ is slightly higher but due to large uncertainties consistent with the measurement based on SDSS DLAs (Noterdaeme et al. 2012) and the combined CORALS and UCSD sample of radio-selected quasars (Jorgenson et al. 2006). Interestingly, the PDLA detection fraction is also a factor of 3 larger. Since the quasars in our sample are fainter than in the previous surveys, there may indeed be a dependence between n_{DLA} and optical faint-

ness of quasars (Ellison et al. 2001). These results also underline the need for larger surveys of dust-unbiased DLAs. Due to limited spectral coverage, we could search for Ly α in only 30% of our SALT-NOT sample presented here. A complete search of Ly α absorption towards all the targets will allow us to examine the above-mentioned excesses at a higher significance level.

Eventually, much larger radio-selected surveys ($\Delta X \gtrsim 10^4$) such as MALS are needed to uncover the population of dusty DLAs. The key science objectives are summarized in Gupta et al. (2017), and the survey is well underway. The first L- and UHF-band spectra based on the science verification data are presented in Gupta et al. (2021) and Combes et al. (2021), respectively. Each MALS pointing is centered at a bright (> 200 mJy at 1 GHz) radio source. Through wide-band spectra of the central bright radio source and the numerous off-axis radio sources, it will sample the column density distribution ($N(\text{HI}) > 5 \times 10^{19} \text{ cm}^{-2}$; $T_s = 100$ K) relevant to characterize the cross-section of cold atomic gas in and around normal galaxies and AGNs at $0 < z < 1.4$. Simultaneously, it will also be sensitive to detect OH main line absorption at $z < 1.9$ in gas with $N(\text{OH}) > 2.4 \times 10^{14} \text{ cm}^{-2}$ (excitation temperature = 3.5 K). Since the formation of OH is tightly coupled to H₂, the measurement of OH cross-section at $z < 2$ will be a crucial input through which to understand the redshift evolution of CNM cross-section (Balashev et al. 2020).

The work presented here is the first to examine the detectability of high- $N(\text{HI})$ absorbers in a MIR selected sample of quasars with searches based on radio / optically selected quasars. Although only one associated H I 21-cm absorber is detected, the slight excess of DLAs and PDLAs in our sample is encouraging and with larger surveys could potentially lead to the estimates of dusty AGNs missed in optically selected surveys (the fraction

could be anywhere between 10-50%; Richards et al. 2003; Glikman et al. 2012). Some of the ongoing work we are pursuing is to understand the impact of MIR selection on the colors of selected quasars. In the near future, we will also present the complete census of DLAs and PDLAs in our sample, and results from the targeted deeper H I 21-cm line observations towards these. As such, this paper presents a crucial step towards a detailed understanding of the high- $N(\text{HI})$ searches at $z > 2$ to be eventually taken up with the low-frequency component of the SKA (Morganti et al. 2015).

We thank the anonymous referee for helpful suggestions. We thank GMRT staff for their support during the observations. GMRT is run by the National Centre for Radio Astrophysics of the Tata Institute of Fundamental Research. This work is based on observations made with SALT and NOT. The uGMRT data were processed using the MALS data processing facility at IUCAA. The CASA package is developed by an international consortium of scientists based at the National Radio Astronomical Observatory (NRAO), the European Southern Observatory (ESO), the National Astronomical Observatory of Japan (NAOJ), the Academia Sinica Institute of Astronomy and Astrophysics (ASIAA), the CSIRO division for Astronomy and Space Science (CASS), and the Netherlands Institute for Radio Astronomy (ASTRON) under the guidance of NRAO. The National Radio Astronomy Observatory is a facility of the National Science Foundation operated under cooperative agreement by Associated Universities, Inc.

Facilities: NOT, SALT and uGMRT

Software: ARTIP (Gupta et al. 2021), Astropy (Astropy Collaboration et al. 2013, 2018), CASA (McMullin et al. 2007) and Matplotlib (Hunter 2007).

REFERENCES

- Adams, J. J., Hill, G. J., & MacQueen, P. J. 2009, ApJ, 694, 314, doi: [10.1088/0004-637X/694/1/314](https://doi.org/10.1088/0004-637X/694/1/314)
- Aditya, J. N. H. S., Jorgenson, R., Joshi, V., et al. 2021, MNRAS, 500, 998, doi: [10.1093/mnras/staa3306](https://doi.org/10.1093/mnras/staa3306)
- Aditya, J. N. H. S., Kanekar, N., & Kurapati, S. 2016, MNRAS, 455, 4000, doi: [10.1093/mnras/stv2563](https://doi.org/10.1093/mnras/stv2563)
- Allison, J. R., Sadler, E. M., & Meekin, A. M. 2014, MNRAS, 440, 696, doi: [10.1093/mnras/stu289](https://doi.org/10.1093/mnras/stu289)
- Allison, J. R., Moss, V. A., Macquart, J.-P., et al. 2017, MNRAS, 465, 4450, doi: [10.1093/mnras/stw2860](https://doi.org/10.1093/mnras/stw2860)
- Astropy Collaboration, Robitaille, T. P., Tollerud, E. J., et al. 2013, A&A, 558, A33, doi: [10.1051/0004-6361/201322068](https://doi.org/10.1051/0004-6361/201322068)
- Astropy Collaboration, Price-Whelan, A. M., Sipőcz, B. M., et al. 2018, AJ, 156, 123, doi: [10.3847/1538-3881/aabc4f](https://doi.org/10.3847/1538-3881/aabc4f)
- Balashev, S., Gupta, N., & Kosenko, D. 2020, arXiv e-prints, arXiv:2012.12241. <https://arxiv.org/abs/2012.12241>
- Baloković, M., Smolčić, V., Ivezić, Ž., et al. 2012, ApJ, 759, 30, doi: [10.1088/0004-637X/759/1/30](https://doi.org/10.1088/0004-637X/759/1/30)

- Bischetti, M., Feruglio, C., Piconcelli, E., et al. 2021, *A&A*, 645, A33, doi: [10.1051/0004-6361/202039057](https://doi.org/10.1051/0004-6361/202039057)
- Borthakur, S., Tripp, T. M., Yun, M. S., et al. 2010, *ApJ*, 713, 131, doi: [10.1088/0004-637X/713/1/131](https://doi.org/10.1088/0004-637X/713/1/131)
- Briggs, F. H., Sorar, E., & Taramopoulos, A. 1993, *ApJ*, 415, L99, doi: [10.1086/187042](https://doi.org/10.1086/187042)
- Brown, R. L., & Roberts, M. S. 1973, *ApJ*, 184, L7
- Burgh, E. B., Nordsieck, K. H., Kobulnicky, H. A., et al. 2003, in *Society of Photo-Optical Instrumentation Engineers (SPIE) Conference Series*, Vol. 4841, Proc. SPIE, ed. M. Iye & A. F. M. Moorwood, 1463–1471
- Carilli, C. L., Menten, K. M., Reid, M. J., Rupen, M. P., & Yun, M. S. 1998, *ApJ*, 494, 175, doi: [10.1086/305191](https://doi.org/10.1086/305191)
- Carilli, C. L., Owen, F. N., & Harris, D. E. 1994, *AJ*, 107, 480, doi: [10.1086/116870](https://doi.org/10.1086/116870)
- Carilli, C. L., & van Gorkom, J. H. 1992, *ApJ*, 399, 373, doi: [10.1086/171934](https://doi.org/10.1086/171934)
- Carilli, C. L., Wang, R., van Hoven, M. B., et al. 2007, *AJ*, 133, 2841, doi: [10.1086/518436](https://doi.org/10.1086/518436)
- Chambers, K. C., Magnier, E. A., Metcalfe, N., et al. 2016, arXiv e-prints, arXiv:1612.05560. <https://arxiv.org/abs/1612.05560>
- Chandola, Y., Saikia, D. J., & Li, D. 2020, *MNRAS*, 494, 5161, doi: [10.1093/mnras/staa1029](https://doi.org/10.1093/mnras/staa1029)
- Combes, F., Gupta, N., Muller, S., et al. 2021, arXiv e-prints, arXiv:2101.00188. <https://arxiv.org/abs/2101.00188>
- Condon, J. J., Cotton, W. D., Greisen, E. W., et al. 1998, *AJ*, 115, 1693, doi: [10.1086/300337](https://doi.org/10.1086/300337)
- Conway, J. E. 2002, *New A Rev.*, 46, 263, doi: [10.1016/S1387-6473\(01\)00191-9](https://doi.org/10.1016/S1387-6473(01)00191-9)
- Curran, S. J., Allison, J. R., Glowacki, M., Whiting, M. T., & Sadler, E. M. 2013, *MNRAS*, 431, 3408, doi: [10.1093/mnras/stt438](https://doi.org/10.1093/mnras/stt438)
- Curran, S. J., & Whiting, M. T. 2010, *ApJ*, 712, 303, doi: [10.1088/0004-637X/712/1/303](https://doi.org/10.1088/0004-637X/712/1/303)
- Cutri, R. M., & et al. 2014, *VizieR Online Data Catalog*, II/328
- Darling, J., Macdonald, E. P., Haynes, M. P., & Giovanelli, R. 2011, *ApJ*, 742, 60, doi: [10.1088/0004-637X/742/1/60](https://doi.org/10.1088/0004-637X/742/1/60)
- Decarli, R., Walter, F., Venemans, B. P., et al. 2018, *ApJ*, 854, 97, doi: [10.3847/1538-4357/aaa5aa](https://doi.org/10.3847/1538-4357/aaa5aa)
- Dutta, R., Srianand, R., & Gupta, N. 2019, *MNRAS*, 489, 1099, doi: [10.1093/mnras/stz2178](https://doi.org/10.1093/mnras/stz2178)
- Dutta, R., Srianand, R., Gupta, N., & Joshi, R. 2017a, *MNRAS*, 468, 1029, doi: [10.1093/mnras/stx538](https://doi.org/10.1093/mnras/stx538)
- Dutta, R., Srianand, R., Gupta, N., et al. 2017b, *MNRAS*, 465, 4249, doi: [10.1093/mnras/stw3040](https://doi.org/10.1093/mnras/stw3040)
- . 2017c, *MNRAS*, 465, 588, doi: [10.1093/mnras/stw2689](https://doi.org/10.1093/mnras/stw2689)
- Ellison, S. L., Yan, L., Hook, I. M., et al. 2001, *A&A*, 379, 393, doi: [10.1051/0004-6361:20011281](https://doi.org/10.1051/0004-6361:20011281)
- Ellison, S. L., York, B. A., Pettini, M., & Kanekar, N. 2008, *MNRAS*, 388, 1349, doi: [10.1111/j.1365-2966.2008.13482.x](https://doi.org/10.1111/j.1365-2966.2008.13482.x)
- Feruglio, C., Fiore, F., Carniani, S., et al. 2018, *A&A*, 619, A39, doi: [10.1051/0004-6361/201833174](https://doi.org/10.1051/0004-6361/201833174)
- Gehrels, N. 1986, *ApJ*, 303, 336, doi: [10.1086/164079](https://doi.org/10.1086/164079)
- Geier, S. J., Heintz, K. E., Fynbo, J. P. U., et al. 2019, *A&A*, 625, L9, doi: [10.1051/0004-6361/201935108](https://doi.org/10.1051/0004-6361/201935108)
- Geréb, K., Maccagni, F. M., Morganti, R., & Oosterloo, T. A. 2015, *A&A*, 575, A44, doi: [10.1051/0004-6361/201424655](https://doi.org/10.1051/0004-6361/201424655)
- Glikman, E., Urrutia, T., Lacy, M., et al. 2012, *ApJ*, 757, 51, doi: [10.1088/0004-637X/757/1/51](https://doi.org/10.1088/0004-637X/757/1/51)
- Glowacki, M., Allison, J. R., Sadler, E. M., et al. 2017, *MNRAS*, 467, 2766, doi: [10.1093/mnras/stx214](https://doi.org/10.1093/mnras/stx214)
- Grasha, K., Darling, J., Bolatto, A., Leroy, A. K., & Stocke, J. T. 2019, *ApJS*, 245, 3, doi: [10.3847/1538-4365/ab4906](https://doi.org/10.3847/1538-4365/ab4906)
- Grasha, K., Darling, J., Leroy, A. K., & Bolatto, A. D. 2020, *MNRAS*, 498, 883, doi: [10.1093/mnras/staa2521](https://doi.org/10.1093/mnras/staa2521)
- Gupta, N., Momjian, E., Srianand, R., et al. 2018a, *ApJ*, 860, L22, doi: [10.3847/2041-8213/aac9cd](https://doi.org/10.3847/2041-8213/aac9cd)
- Gupta, N., & Saikia, D. J. 2006, *MNRAS*, 370, 738, doi: [10.1111/j.1365-2966.2006.10498.x](https://doi.org/10.1111/j.1365-2966.2006.10498.x)
- Gupta, N., Salter, C. J., Saikia, D. J., Ghosh, T., & Jeyakumar, S. 2006, *MNRAS*, 373, 972, doi: [10.1111/j.1365-2966.2006.11064.x](https://doi.org/10.1111/j.1365-2966.2006.11064.x)
- Gupta, N., Srianand, R., Bowen, D. V., York, D. G., & Wadadekar, Y. 2010, *MNRAS*, 408, 849, doi: [10.1111/j.1365-2966.2010.17198.x](https://doi.org/10.1111/j.1365-2966.2010.17198.x)
- Gupta, N., Srianand, R., Petitjean, P., et al. 2012, *A&A*, 544, A21, doi: [10.1051/0004-6361/201219159](https://doi.org/10.1051/0004-6361/201219159)
- Gupta, N., Srianand, R., Petitjean, P., Noterdaeme, P., & Saikia, D. J. 2009, *MNRAS*, 398, 201, doi: [10.1111/j.1365-2966.2009.14933.x](https://doi.org/10.1111/j.1365-2966.2009.14933.x)
- Gupta, N., Srianand, R., Baan, W., et al. 2017, *ArXiv e-prints*. <https://arxiv.org/abs/1708.07371>
- Gupta, N., Srianand, R., Farnes, J. S., et al. 2018b, *MNRAS*, 476, 2432, doi: [10.1093/mnras/sty384](https://doi.org/10.1093/mnras/sty384)
- Gupta, N., Jagannathan, P., Srianand, R., et al. 2021, *ApJ*, 907, 11, doi: [10.3847/1538-4357/abcb85](https://doi.org/10.3847/1538-4357/abcb85)
- Heiles, C., & Troland, T. H. 2003, *ApJ*, 586, 1067, doi: [10.1086/367828](https://doi.org/10.1086/367828)
- Hunter, J. D. 2007, *Computing in Science and Engineering*, 9, 90, doi: [10.1109/MCSE.2007.55](https://doi.org/10.1109/MCSE.2007.55)
- Jorgenson, R. A., Wolfe, A. M., Prochaska, J. X., et al. 2006, *ApJ*, 646, 730, doi: [10.1086/505130](https://doi.org/10.1086/505130)

- Kanekar, N., Chengalur, J. N., & Lane, W. M. 2007, *MNRAS*, 375, 1528, doi: [10.1111/j.1365-2966.2007.11430.x](https://doi.org/10.1111/j.1365-2966.2007.11430.x)
- Kanekar, N., Prochaska, J. X., Smette, A., et al. 2014, *MNRAS*, 438, 2131, doi: [10.1093/mnras/stt2338](https://doi.org/10.1093/mnras/stt2338)
- Kobulnicky, H. A., Nordsieck, K. H., Burgh, E. B., et al. 2003, in *Society of Photo-Optical Instrumentation Engineers (SPIE) Conference Series*, Vol. 4841, *Instrument Design and Performance for Optical/Infrared Ground-based Telescopes*, ed. M. Iye & A. F. M. Moorwood, 1634–1644
- Krogager, J.-K., Fynbo, J. P. U., Møller, P., et al. 2019, *MNRAS*, 486, 4377, doi: [10.1093/mnras/stz1120](https://doi.org/10.1093/mnras/stz1120)
- Krogager, J. K., Fynbo, J. P. U., Noterdaeme, P., et al. 2016, *MNRAS*, 455, 2698, doi: [10.1093/mnras/stv2346](https://doi.org/10.1093/mnras/stv2346)
- Krogager, J.-K., & Noterdaeme, P. 2020, *A&A*, 644, L6, doi: [10.1051/0004-6361/202039843](https://doi.org/10.1051/0004-6361/202039843)
- Krogager, J. K., Gupta, N., Noterdaeme, P., et al. 2018, *ApJS*, 235, 10, doi: [10.3847/1538-4365/aaab51](https://doi.org/10.3847/1538-4365/aaab51)
- Lacy, M., Baum, S. A., Chandler, C. J., et al. 2020, *PASP*, 132, 035001, doi: [10.1088/1538-3873/ab63eb](https://doi.org/10.1088/1538-3873/ab63eb)
- Lawrence, C. R., Cohen, J. G., & Oke, J. B. 1995a, *AJ*, 110, 2583, doi: [10.1086/117714](https://doi.org/10.1086/117714)
- Lawrence, C. R., Elston, R., Januzzi, B. T., & Turner, E. L. 1995b, *AJ*, 110, 2570, doi: [10.1086/117713](https://doi.org/10.1086/117713)
- Maccagni, F. M., Morganti, R., Oosterloo, T. A., Geréb, K., & Maddox, N. 2017, *A&A*, 604, A43, doi: [10.1051/0004-6361/201730563](https://doi.org/10.1051/0004-6361/201730563)
- Manti, S., Gallerani, S., Ferrara, A., Greig, B., & Feruglio, C. 2017, *MNRAS*, 466, 1160, doi: [10.1093/mnras/stw3168](https://doi.org/10.1093/mnras/stw3168)
- Martini, P., & Weinberg, D. H. 2001, *ApJ*, 547, 12, doi: [10.1086/318331](https://doi.org/10.1086/318331)
- McMullin, J. P., Waters, B., Schiebel, D., Young, W., & Golap, K. 2007, in *Astronomical Society of the Pacific Conference Series*, Vol. 376, *Astronomical Data Analysis Software and Systems XVI*, ed. R. A. Shaw, F. Hill, & D. J. Bell, 127
- Momjian, E., Carilli, C. L., Bañados, E., Walter, F., & Venemans, B. P. 2018, *ApJ*, 861, 86, doi: [10.3847/1538-4357/aac76f](https://doi.org/10.3847/1538-4357/aac76f)
- Moore, C. B., Carilli, C. L., & Menten, K. M. 1999, *ApJ*, 510, L87, doi: [10.1086/311818](https://doi.org/10.1086/311818)
- Morganti, R., & Oosterloo, T. 2018, *A&A Rev.*, 26, 4, doi: [10.1007/s00159-018-0109-x](https://doi.org/10.1007/s00159-018-0109-x)
- Morganti, R., Sadler, E. M., & Curran, S. 2015, *Advancing Astrophysics with the Square Kilometre Array (AASKA14)*, 134. <https://arxiv.org/abs/1501.01091>
- Noterdaeme, P., Balashev, S., Krogager, J. K., et al. 2019, *A&A*, 627, A32, doi: [10.1051/0004-6361/201935371](https://doi.org/10.1051/0004-6361/201935371)
- Noterdaeme, P., Ledoux, C., Zou, S., et al. 2018, *A&A*, 612, A58, doi: [10.1051/0004-6361/201732266](https://doi.org/10.1051/0004-6361/201732266)
- Noterdaeme, P., Petitjean, P., Carithers, W. C., et al. 2012, *A&A*, 547, L1, doi: [10.1051/0004-6361/201220259](https://doi.org/10.1051/0004-6361/201220259)
- Petitjean, P., Srianand, R., & Ledoux, C. 2000, *A&A*, 364, L26
- Prochaska, J. X., Chen, H.-W., Wolfe, A. M., Dessauges-Zavadsky, M., & Bloom, J. S. 2008a, *ApJ*, 672, 59, doi: [10.1086/523689](https://doi.org/10.1086/523689)
- Prochaska, J. X., Hennawi, J. F., & Herbert-Fort, S. 2008b, *ApJ*, 675, 1002, doi: [10.1086/526508](https://doi.org/10.1086/526508)
- Rao, S. M., Turnshek, D. A., & Nestor, D. B. 2006, *ApJ*, 636, 610, doi: [10.1086/498132](https://doi.org/10.1086/498132)
- Reeves, S. N., Sadler, E. M., Allison, J. R., et al. 2016, *MNRAS*, 457, 2613, doi: [10.1093/mnras/stv3011](https://doi.org/10.1093/mnras/stv3011)
- Richards, G. T., Hall, P. B., Vanden Berk, D. E., et al. 2003, *AJ*, 126, 1131, doi: [10.1086/377014](https://doi.org/10.1086/377014)
- Saxena, A., Marinello, M., Overzier, R. A., et al. 2018, *MNRAS*, 480, 2733, doi: [10.1093/mnras/sty1996](https://doi.org/10.1093/mnras/sty1996)
- Selsing, J., Fynbo, J. P. U., Christensen, L., & Krogager, J. K. 2016, *A&A*, 585, A87, doi: [10.1051/0004-6361/201527096](https://doi.org/10.1051/0004-6361/201527096)
- Shukla, G., Srianand, R., Gupta, N., et al. 2021, *MNRAS*, 501, 5362, doi: [10.1093/mnras/staa3977](https://doi.org/10.1093/mnras/staa3977)
- Srianand, R., Gupta, N., Momjian, E., & Vivek, M. 2015, *MNRAS*, 451, 917, doi: [10.1093/mnras/stv1004](https://doi.org/10.1093/mnras/stv1004)
- Srianand, R., Gupta, N., Petitjean, P., et al. 2012, *MNRAS*, 421, 651, doi: [10.1111/j.1365-2966.2011.20342.x](https://doi.org/10.1111/j.1365-2966.2011.20342.x)
- Srianand, R., Gupta, N., Petitjean, P., Noterdaeme, P., & Saikia, D. J. 2008, *MNRAS*, 391, L69, doi: [10.1111/j.1745-3933.2008.00558.x](https://doi.org/10.1111/j.1745-3933.2008.00558.x)
- Srianand, R., Gupta, N., Rahmani, H., et al. 2013, *MNRAS*, 428, 2198, doi: [10.1093/mnras/sts190](https://doi.org/10.1093/mnras/sts190)
- Uson, J. M., Bagri, D. S., & Cornwell, T. J. 1991, *Phys. Rev. Lett.*, 67, 3328, doi: [10.1103/PhysRevLett.67.3328](https://doi.org/10.1103/PhysRevLett.67.3328)
- Venemans, B. P., Walter, F., Decarli, R., et al. 2017, *ApJ*, 851, L8, doi: [10.3847/2041-8213/aa943a](https://doi.org/10.3847/2041-8213/aa943a)
- Vermeulen, R. C., Pihlström, Y. M., Tschager, W., et al. 2003, *A&A*, 404, 861, doi: [10.1051/0004-6361:20030468](https://doi.org/10.1051/0004-6361:20030468)
- Weedman, D., Sargsyan, L., Leboutteiller, V., Houck, J., & Barry, D. 2012, *ApJ*, 761, 184, doi: [10.1088/0004-637X/761/2/184](https://doi.org/10.1088/0004-637X/761/2/184)
- Wolfe, A. M., Briggs, F. H., & Jauncey, D. L. 1981, *ApJ*, 248, 460, doi: [10.1086/159170](https://doi.org/10.1086/159170)
- Wright, E. L., Eisenhardt, P. R. M., Mainzer, A. K., et al. 2010, *AJ*, 140, 1868, doi: [10.1088/0004-6256/140/6/1868](https://doi.org/10.1088/0004-6256/140/6/1868)
- York, D. G., Adelman, J., Anderson, John E., J., et al. 2000, *AJ*, 120, 1579, doi: [10.1086/301513](https://doi.org/10.1086/301513)